Stony Brook University

Modeling Platelets on Parallel Computers

A Dissertation Presented

by

Seetha Pothapragada

to

The Graduate School

in Partial Fulfillment of the

Requirements

for the Degree of

Doctor of Philosophy

in

Applied Mathematics and Statistics

Stony Brook University

May 2015

Stony Brook University

The Graduate School

Seetha Pothapragada

We, the dissertation committee for the above candidate for the

Doctor of Philosophy degree, hereby recommend

acceptance of this dissertation.

Dr. Yuefan Deng – Dissertation Advisor
Professor, Department of Applied Mathematics and Statistics

Dr. Wei Zhu - Chairperson of Defense
Professor, Department of Applied Mathematics and Statistics

Dr. Danny Bluestein - Committee Member
Professor, Department of Biomedical Engineering

Dr. Shmuel Einav - Committee Member
Professor, Department of Biomedical Engineering

This dissertation is accepted by the Graduate School

Charles Taber

Dean of the Graduate School

Abstract of the Dissertation

Modeling Platelets on Parallel Computers

by

Seetha Pothapragada

Doctor of Philosophy

in

Applied Mathematics and Statistics

Stony Brook University

2015

Mechanical Heart Valves (MHV) provides life-saving solutions to patients suffering from cardiovascular diseases. But these devices are often plagued by non-physiological flow patterns resulting in increased shear stress conditions. This leads to platelet damage, a precursor of thromboembolism, thus impeding the device usability and demanding lifelong anticoagulation treatments. While the flow and stresses are in the micron level, the platelet behavior is at the nm level, thus presenting a major computational challenge for simulating this multiscale multi-physics modeling problem. This dissertation focuses on using parallel computers to develop a computational framework based on n-particle simulations, defined by Coarse Grained Molecular Dynamics (CGMD) for platelets and Dissipative Particle Dynamics (DPD) for fluids.

First, the problem of developing a three-dimensional (3D) platelet model to characterize the filopodia formation observed during activation is considered. This CGMD particle-based model can deform to emulate the complex shape change and filopodia formation that platelets

undergo during activation. The model represents the phenomenological functions of the three platelet cellular zones; peripheral, structural and organelle, by bonded and non-bonded particles. By exploring the parameter space of this CGMD model, successful simulations of the dynamics of varied filopodia formation on platelets is demonstrated.

Second, a quantitative model for platelet morphological change that considers filopodial dynamics, circularity of the central body and average filopod number is presented. Derived from the logistic equation, the morphological change is expressed as a mathematical function of mechanical shear stress and exposure time and this quantitative model for the overall platelet morphology is corroborated with *in vitro* experiments. The model for the first time enables a quantitative analysis of platelet morphology during early stages of activation and offers insights into the underlying effects of mechanical shear stresses over time on platelet morphology.

In loving memory of my mother, greatest influence on my life,

Late. Kasturi Pothapragada

Table of Contents

Contents

List of Tables

List of Figures

List of Abbreviations

3D	Three-Dimensional
ADP	Adenosine Diphosphate
CFD	Computational Fluid Dynamics
CG	Coarse Grained
CGMD	Coarse Grained Molecular Dynamics
DEM	Discrete Element Method
DPD	Dissipative Particle Dynamics
ENIAC	Electronic Numerical Integrator and Computer
FEM	Finite Element Methods
Flops	Floating Point Operations per Second
HPC	High Performance Computing
HSD	Hemodynamic Shearing Device
LAMMPS	Large-scale Atomic/Molecular Massively Parallel Simulator
LBM	Lattice-Boltzmann Method
LJ	Lennard-Jones
MANIAC	Mathematical Analyzer, Integrator and Computer

MC	Monte Carlo methods
MD	Molecular Dynamics
MFT	Mean Field Theory
MHV	Mechanical Heart Valve
NAMD	Not (just) Another Molecular Dynamics
OCS	Open Canalicular System
PAS	Platelet Activation State
PBC	Periodic Boundary Condition
PDEs	Partial Differential Equations
RBCs	Red Blood Cells
SA	Stress Accumulation
SEM	Scanning Electron Microscopy
SPH	Smooth Particle Hydrodynamics
TXA_2	Thromboxane
VMD	Visual Molecular Dynamics

Acknowledgments

I owe my gratitude to all the people who have made this thesis possible and because of whom my graduate experience has been one that I will cherish forever.

First and foremost, I would like to thank my advisor, Professor Yuefan Deng for giving me the opportunity to work with him. Without his supervision, advice and guidance at every stage of my graduate career, this work would not be possible. It has been a pleasure to work with and learn from such an extraordinary individual. I am also most grateful to Professor Danny Bluestein, who is like a co-advisor to me. The gratitude I have for his support and tutelage is impossible to quantify. I am also thankful to Professor Wei Zhu and Professor Shmuel Einav for agreeing to be a part of committee; their comments on my thesis are invaluable.

I would like to thank my friends at Deng's lab and Bluestein's Biofluids lab for providing a friendly scientific atmosphere. The collaboration between the two teams enabled easy communication between applied mathematicians and biologists. Special thanks to Dr. Jawaad Sheriff for conducting experiments at Dr. Bluestein's lab and providing valuable images that helped in my research.

I am also thankful for my pillars of support, dad *Krishna Rao* and brother *Sriharsha*, and their unwavering belief in me, without which I could not have completed my studies. I am forever blessed to have met my fiancé, *Girish Ramakrishnan*, at Stony Brook, whose love and companionship mean the world to me. I also admire his patience for reading through my thesis.

The text of this dissertation in part is a reprint of the materials as it appears in [1, 2].

Publications

Journal Publications

[1] **Pothapragada, S.**, Zhang, P., Sheriff, J., Livelli, M., Slepian, M.J., Deng, Y., Bluestein, D., "A Phenomenological Particle-Based Platelet Model for Simulating Filopodia Formation during Early Activation", International Journal for Numerical Methods in Biomedical Engineering, 2015. *DOI: 10.1002/cnm.2702*

[2] **Pothapragada, S.**, Sheriff, J., Bluestein, D., Deng, Y., "A Quantitative Model for Shear Flow-Induced Platelet Morphological Changes and Corroboration with In Vitro Experiments", Mathematical Biosciences (Under Review, Jan 2015)

Conference Proceedings

[3] **Pothapragada, S.**, Y. Deng. "Supercomputer simulations of platelet activation in blood plasma at multiple scales". in International Conference on High Performance Computing & Simulation (HPCS), Bologna, Italy, 2014. *DOI: 10.1109/HPCSim.2014.6903802*

[4] Bluestein, D., Soares, J.S., Zhang, P., Gao, C., **Pothapragada, S.**, Zhang, N., Slepian, M.J., Deng, Y. "Multiscale Modeling of Flow Induced Thrombogenicity with Dissipative Particle Dynamics (DPD) and Molecular Dynamics (MD)." in Proceedings of the ASME/FDA 2013 1st Annual Frontiers in Medical Devices: Applications of Computer Modeling and Simulation FMD 2013, Washington, D.C., September 11-13, 2013. *DOI: 10.1115/FMD2013-16176*

[5] Zhang, P., Sheriff, J., Soares, J.S., Gao, C., **Pothapragada, S.**, Zhang, N., Deng, Y., Bluestein, D. "Multiscale Modeling of Flow Induced Thrombogenicity Using Dissipative Particle Dynamics and Coarse Grained Molecular Dynamics." in Proceedings of the ASME 2013 Summer Bioengineering Conference, Sunriver, Oregon, June 26-29, 2013. *DOI: 10.1115/SBC2013-14187*

[6] Bluestein, D., Soares, J.S., Zhang, P., Gao, C., **Pothapragada, S.**, Zhang, N., Slepian, M.J., Deng, Y. "Multiscale Modeling of Flow Induced Thrombogenicity Using Dissipative Particle Dynamics and Molecular Dynamics," ASME 2013 2nd Global Congress on NanoEngineering for Medicine and Biology, Boston, Massachusetts, USA, February 4–6, 2013. *DOI: 10.1115/NEMB2013-93094*

Chapter 1

Introduction

Supercomputers are the strong arms of the technological world. They have a computing power tens of thousands of time faster than traditional desktop and cost tens of millions of dollars. They take up entire rooms and need to be continuously cooled to prevent overheating. They have thousands of processor cores and perform thousands of trillions of calculations per second. Such kind of power enables supercomputers to tackle big scientific problems spanning wide spatial scales, from uncovering the origins of the universe to delving into the atomic level structural details of materials. For example, in the field of astronomy, supercomputers are helping physicists in recreating realistic models of the Big Bang [7] by performing thousand trillion calculations per second. Supercomputers are also widely used in studying protein folding, where the protein form and plays a significant role on a person's health. One protein mis-fold can lead to Mad Cow disease, Alzheimer's disease or cystic fibrosis. IBM's BlueGene supercomputer [8] has helped uncover the folding strategies of different proteins and enabling the process of curing such kinds of diseases. In nuclear science, Sequoia supercomputer [9], a 20 petaflops (peta=10^{15}, Flops – Floating point operations per second) machine, situated at the Lawrence Livermore National Laboratory is used to simulate nuclear explosions to replace real-world nuke testing. In weather forecasting, supercomputing simulations not only predict the hurricane path [10] but also are

capable of modeling vulnerable power stations and electrical lines and aide officials in safe evacuation of residents.

Supercomputers are also used to study the human body. They are really good at computation: It would take approximately 100 billion people each with a calculator about 50 years to do what a petaflop supercomputer can do in a day. But human brains surpass supercomputers with their ability to process information by doing many calculations in parallel. Last year, the K supercomputer in Japan [11] is able to simulate one second human brain activity in 40 minutes. With such feats that test the limits of the latest simulation technology, one can get a glimpse of the possible achievements by the next generation of supercomputers – termed as 'exascale computing'.

1.1 Motivations

Until recently, advances of computational sciences have had little impacts on life and medical research projects. With today's supercomputers (Tianhe-2) that are capable of performing 10^{16} Flops, life science researchers are able to look forward to quantitative models that computational community is able to deliver with less and less compromising assumptions about such models. In medical research, organs made of real cells and proteins that were impossible to model at appreciable spatial and temporal scales are now simulated on supercomputers and provide researchers valuable insights. Each biological scale, starting from organism, organ, tissue, cell, protein to DNA has been successfully modeled separately. Now, scientists and mathematicians are unifying their strengths to tackle all of these layers into a single multi-scale more realistic model.

One such example of multiscale modeling in physiology is the simulation of the blood flow through the blood vessels controlled by the heart. Inflammation or damage on blood vessel walls lead to clot formation called a thrombus. At the device level, thrombus formation is at the core of many complicated cardiovascular diseases and is leading cause of death in the developed world. Although implantable blood recirculating devices provide lifesaving solutions to patients, they are also often plagued by thromboembolic complications and require complex anticoagulation regimes. At the cellular level, platelets that flow freely in blood are recruited to the site of injured wall and are the building blocks of thrombosis. Platelets that normally look like smooth thin disks in flow, upon sensing an injured wall, get "activated" and turn into sticky spiny cells that adhere and form a clot. Recently, it has been discovered that platelets get activated not only by chemical signals but also due to mechanical signals caused by pathological shear flow patterns in blood recirculating devices. This sudden change of platelet shape is very hard to quantify and parameterize and is therefore computationally challenging. None of the numerical simulations modeled by mathematicians and engineers can account for the sudden change in shape and properties of flowing particles.

This dissertation focuses on introducing, for the first time, a platelet model that is able to depict the complex shape changes in response to external shear blood flow and is also computationally efficient to use in multiscale modeling.

1.2 Contributions

This dissertation presents a new mathematical model of a platelet at the bottom/cellular scale, to be used in a multiscale numerical approach for platelet-mediated thrombosis in cardiovascular diseases and devices. The first part of the study considered the particle-based coarse-grained molecular dynamics (CGMD) modeling of the platelet in the quiescent and early-stage activation states. The objectives of this study were of two folds. First, the important cellular sub-components of the platelet including membrane, filamentous core, filament bundles and cytoplasm by particles interacting with simple interaction potentials are presented. Second, simulations of the growth of filopodia, a key feature of the platelet shape change observed during early stages of activation is shown. Also the computational efficiency of this model on high performance computing (HPC) resources is analyzed, as part of the thesis work.

In the second part of the research, a quantitative model that describes the shape change of platelet due to mechanical stresses applied by the blood plasma flow is devised. Real time dynamic microscopy images of platelets exposed to various combinations of shear stress-exposure time in circulation micro channels are studied and a platelet shape change database is established. This database consisting of shear stress, exposure time, platelet diameter, number of filopodia and filopodia lengths is analyzed. The relationship between platelet morphology and external stimuli is derived and this relationship in conjunction with the CGMD platelet when immersed in particulate blood plasma flow represented by the DPD can be used to simulate platelet activation under shear flow conditions.

1.3 Organization

Given below is the brief overview of the thesis.

Chapter 2 describes the basic biological background for the supercomputing application as studied in Chapters 4 and 5. The information provided here allows the interested reader to get a broad impression of the multiscale nature of the work done in this thesis.

Chapter 3 is the overview and background of the numerical methods. More details of system setup, simulation parameters along with other technical information can be found in relevant chapters.

Chapter 4 introduces the coarse-grained (CG) particle-based platelet model. The interaction potentials and the subsequent parameterization are discussed in detail. Use of this novel model to simulate the dynamic filopodia formation is demonstrated. The simulated results are verified by comparing them with well-established laboratory experiments. The simulation performance of this CGMD platelet model on the supercomputing platforms shows that it can represent a platelet with high fidelity and aide in the reducing the computational challenges faced in the multiscale approach.

Chapter 5 presents a study of the platelet's morphology. Platelets undergo dynamic shape change during activation under shear stress flows. When platelets are activated, the most observable phenomena are the growth of filopodia. The filopodia on different platelets act like sensors detecting their environment and also interact with each other. The relationship between the mechanical stimuli caused by the shear flows and the filopodia growth on platelets is investigated,

and represented by a quantitative model. This quantitative model is derived from the well-known Verhulst logistic equation. This model can be used in multiscale simulations of platelet activation where the external shear flow is represented by the DPD and the platelet is modeled by the CGMD to be described as Chapter 4.

Chapter 6 contains the technical summary and discussions of the thesis and outlines the future of this line of research.

Chapter 2

Physiology of Human Platelets

Platelets are simple subcellular fragments that flow in blood, lack nucleus and have clear cytoplasm. Platelets are about 20% of diameter of red blood cells (RBCs), the dominant cell (by volume) in blood. The concentration of platelets in blood is between 150,000 and 450,000 per microliter [12], but due to their size, they make up only a tiny fraction of blood volume. Platelets' principle role is to prevent bleeding. In this chapter, the basic physiological background of a platelet and its activation is described.

2.1 Structure of a Platelet

Platelets are discoid-shaped plates with an average diameter of 3μm and thickness of 0.5μm [13]. Their morphological structure (see Figure 2.1) can be classified into three zones: peripheral, structural and organelle. The peripheral zone consists of a phospholipid bilayer membrane (thickness of 100 A) and an exterior coat (thickness of 150 A-200 A). The bilayer membrane system has an open canalicular system (OCS) that serve as a pathway for transport of substances into the platelet and an membrane enclosed organelle called the dense tubular system [14]. The structural zone has a cytoskeletal assembly with two key components: (a) an actin-based space-filling spoke-like arrangement with the 3D actin cortex at the center and the actin filaments as the spokes [15, 16] and (b) a spectrin-based membrane skeleton. It also contains a peripheral

microtubule coil that confers the discoid shape of the platelet. The organelle zone is an inhomogeneous gel-like cytoplasm with few dense bodies, granules, mitochondria, and lysosomes.

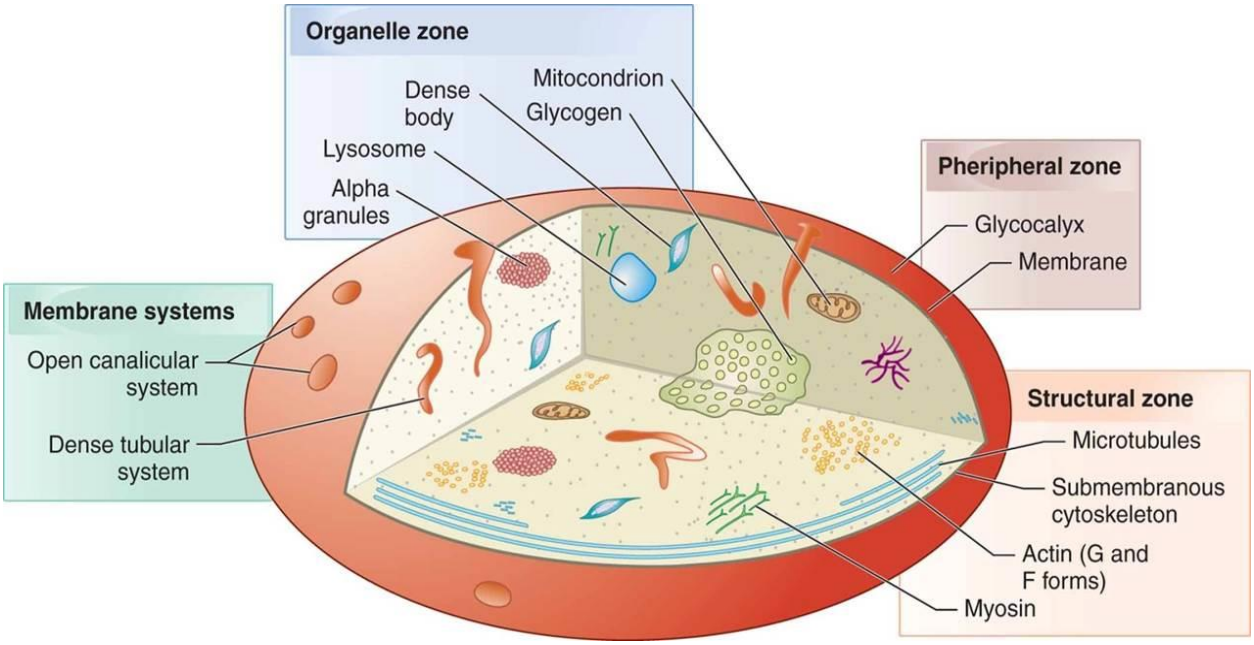

Figure 2.1: Schematic of a platelet structure with all the three zones. The three zones are peripheral, structural and organelle zones. Also shown is the membrane system. Note: Actin network is not represented in this image. (Source: McKenzie, S.B., Clinical laboratory hematology [17])

2.2 Lifespan and Function of a Platelet

Platelets along with other important components of blood, RBCs and white blood cells (WBC) are produced in the bone marrow. Megakaryocytes, large bone marrow cells, develop into giant cells and undergo a fragmentation process to release 1000 platelets (per megakaryocyte). Platelets are thus not true cells in the usual sense, but merely circulating fragments of cells. Once released, platelets circulate in blood for 7 to 10 days [13, 14]. Because of their size and lightweight,

they are pushed out from the center of flowing blood towards the outside and the blood vessel wall. Blood vessel wall is made of endothelium that normally will not allow anything to stick to it, but in the event of an injury or a cut to the vessel wall, the wall contracts a little and the exposed underlying fibers attract the platelets through mechano-chemical signals. Platelets react by changing their shape, extending long arms called filopodia, becoming sticky, coming together and adhering to these fibers and effectively developing a platelet-plug. The platelet-plug forms a strong clot thereby preventing any further loss of RBCs and blood plasma. This sequence of steps of vascular wall contraction, platelet plug formation and clotting is commonly known as hemostasis [18].

2.3 Shape Change of a Platelet and Thrombosis

Clots are also formed when blood flows inside a blood vessel in the cardiovascular system. This process of clotting is called thrombosis and a clot usually dissolves spontaneously. If it doesn't, however, the thrombus can dislodge, transport with blood flow, attach to other pieces of debris with which it comes in contact along the way, eventually travelling to small artery downstream and block blood flow to a vital organ [19]. R. Virchow has proposed the Virchow's triad [20], identifying the three broad categories that are thought to contribute to thrombosis:

1) Changes in blood composition
2) Changes in vessel wall
3) Changes in blood flow

The framework provided by Virchow is still used for understanding hemostasis and thrombosis in a clinical environment. To alleviate the effects of cardiovascular diseases, such as valvular disease and heart failure, particularly among the elderly population, blood recirculation devices are providing a life-saving alternative. Blood recirculating devices include prosthetic heart valves, such as MHVs, and mechanical circulatory support implants, such as ventricular assist devices, total artificial heart, etc. The first two factors of Virchow's triad, in the context of platelet's role and thrombosis, in such blood-contacting devices are well understood [21, 22]. However, the third factor, rheological conditions-the flow-is yet to be fully understood ([23] and references within).

Platelet participates in hemostasis and thrombosis by interplaying between three modes: activation, adhesion and aggregation [24]. Activation can occur as a response to either chemical or mechanical agonists. Chemical agonists primarily include Adenosine diphosphate (ADP), thrombin, thromboxane (TXA_2) and collagen [25]. Mechanical agonists primarily include blood flow-induced shear stress [26, 27]. During activation, platelets in suspension change their shape and rapidly extend filopodia [13]. Filopodia are formed due to the cytoskeletal rearrangement in the structural zone of the platelet (Figure 2.2) that begins within a few seconds and completes within one minute of exposure to agonists [28]. The filopodia on platelets enable them to contact and interact with other platelets in their surroundings, thus stimulating the activation process further. The liberated ADP and TXA_2 during the activation process make the surrounding platelets sticky, and the stickiness of the newly recruited and activated platelets cause them to adhere to each other. When activated platelets bind to each other, it is called aggregation and is an important

step in formation of clot. When activated platelets bind to the vessel wall made of endothelium it is known as adhesion.

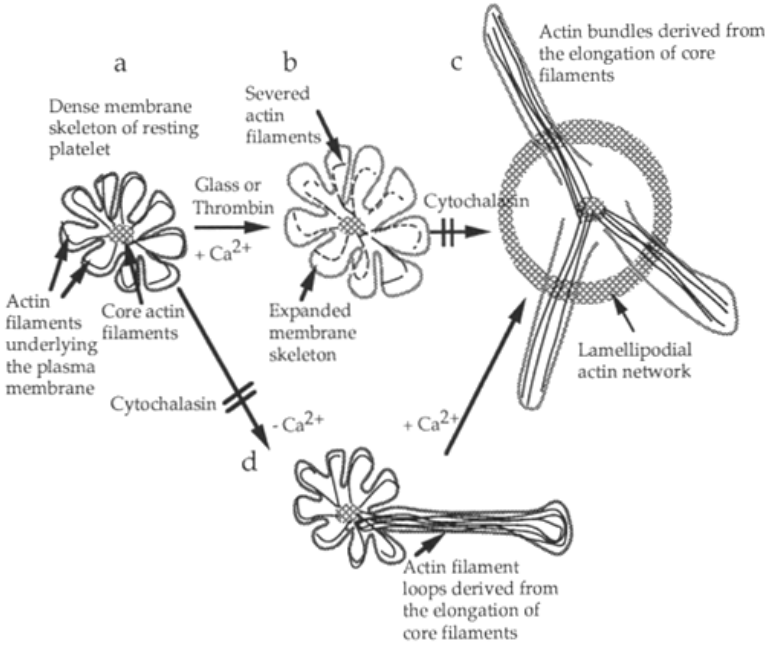

Figure 2.2: Illustration of the structural zone. Cytoskeletal rearrangement occurs during activation. (a) Spoke-like 3D assembly of actin filaments with a central core and radial filaments connected to the membrane through spectrin. (b) Severing of radial filaments from membrane. (c) Filopodia formation due to actin assembly from the central core. (Source: Hartwig, 1992 [16]).

Flow-induced device thrombogenecity is a complex problem that needs to be analyzed at different length and time scales. Using purely experimental and clinical data to study and understand this multiscale problem possesses many practical technical and quantification issues. First, the underlying physico-chemical dynamics in the micro and nano regimes where most of the platelet shape change and activation occurs are exceptionally difficult to capture experimentally. Second, to separate the specific mechanisms involved, *e.g.*, purely chemical or mechanical is challenging. Third, human platelets are highly sensitive and require complex experimental

apparatus to merely isolate them for observation. Fourth, it is almost impossible to study and track individual microscopic platelets in flow, even with the current (2015) cameras at the highest frame rates.

Due to the difficulties of performing conventional laboratory experiments on human platelets, new and additional attention is devoted to the numerical studies in recent years thanks to the advances in computing powers. Computational methods are becoming increasingly popular by which one can systematically isolate specific mechanisms to gain significant understanding of the important control parameters governing the multiscale system. Through large-scale computations, one can tune the important modeling parameters to achieve optimal performance, providing insights for future laboratory experiments. One of the most important advantages of computational methods in biomedical research is that scientists may be able to predict how such systems perform before in-vivo animal trials or clinical tests. Also, accurate simulation results for different kinds of tiny multiscale applications without the need of sophisticate and expensive measuring instruments can be achieved. Another attractive feature of numerical modeling is the capability to account for the relation between microstructural remodeling inside the cell and the overall mechanical behavior in response to their surroundings.

Chapter 3

Algorithms for Numerical Studies of Platelets

Computer simulation as an interdisciplinary tool for solving complex scientific problems on different length and time scales has become indispensable in modern research. Simulations can study super nova explosions and quantum fluctuations of elementary particles like Hadron. Structural hierarchy and process at different length and time scales dictate the determination of different properties and special simulation techniques and physical laws at such scales determine efficient modeling of a system. Section 3.1 discusses the need for numerical modeling of platelet shape change while Section 3.2 provides a short overview of the hierarchy of length scales common in numerical modeling. Section 3.3 discusses the merits of using CGMD to model the platelet and the general algorithm for CGMD implementation on supercomputers. Section 3.4 introduces the simulation software packages used in this thesis. Lastly, section 3.5 briefly describes the evolution of supercomputer simulations and the supercomputing platforms used in this thesis.

3.1 Need for Numerical Modeling

The platelet shape change ultimately leading to device thrombogenecity occurs at multiple lengths and time scales (Figure 3.1). Device thrombogenecity ensues at the length scale of centimeters (O(cm), *i.e.*, order of centimeters) as a result of device geometry etc. Such unnatural conditions might cause turbulence, eddies, recirculation, flow shear stresses and vortices in the

blood flow through and around these devices. These unwanted but incidental pathological conditions occurring at the length scale of millimeters (O(mm)) lead to transport of platelets and agonists that cause platelet activation and clotting. Hence, platelets undergo elevated flow-induced stresses for extended exposure/residence times. Also, there is an increased probability of platelet-wall and platelet-platelet collisions. This leads to activation of platelets at the length scale of micrometers (O(μm)) and platelets change their shape by extending filopodia. Filopodia extension is caused by rearrangement of subcellular components of platelets occurring at the order of nanometers (O(nm)). The release of agonists from such activated platelets initiates the coagulation cascade activating the nearby platelets, leading to platelet aggregation, and eventually, device thrombogenecity.

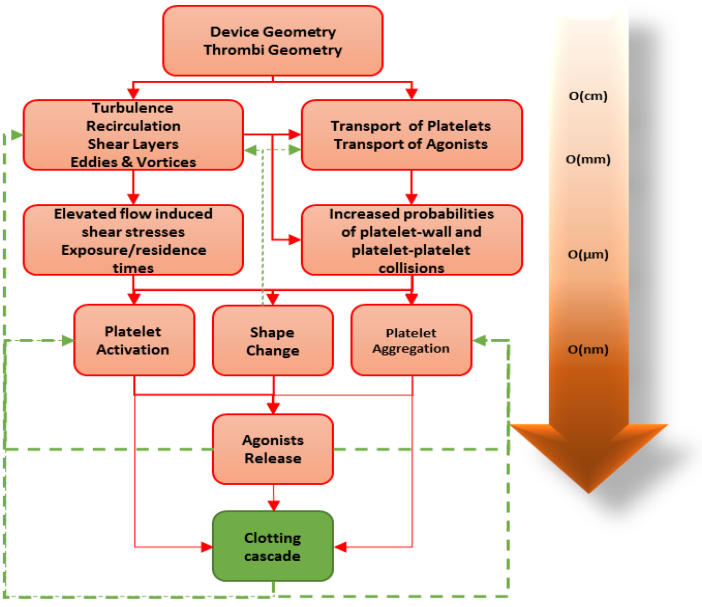

Figure 3.1: Flowchart of multiscale flow-induced thrombosis, including mechanical and biochemical interactions.

3.2 Problems at Multiple Scales

Computational modeling at relevant length and time scales is shown in Figure 3.2. The atomistic quantum scale (nanometers) is modeled by quantum mechanics; the microscopic scale (from nano to micrometers) is modeled by Molecular Dynamics (MD), the intermediate mesoscopic scale (micrometers) is modeled by Mesoscopic CG Methods, and the scale of macroscopic structures (centimeters and meters) is modeled by Continuum Methods.

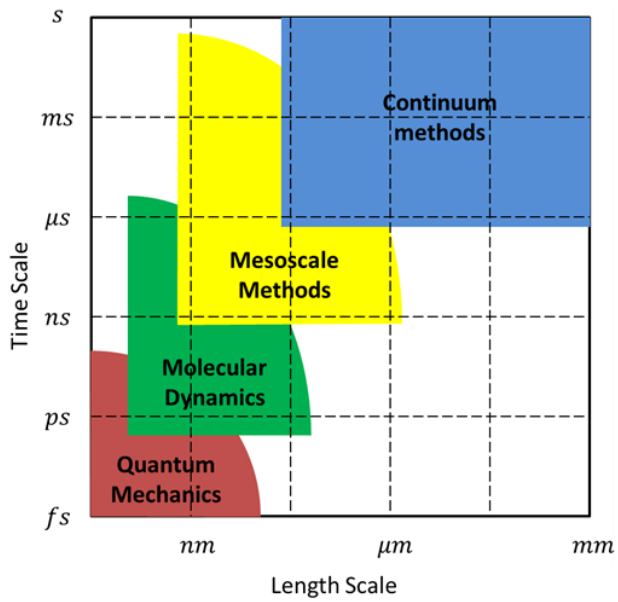

Figure 3.2: A schematic of modeling at multiple length and time scales.

3.2.1 Nanoscale

The sub-atomic electronic structure of any material dictates the molecular geometry, chemistry, quantum mechanical background etc. Modeling at this scale involves taking into account electron-electron interactions and all degrees of freedom of electrons explicitly.

Interaction of electrons can be accurately represented by solving Schrödinger equation (also known as *ab-initio methods*) based on Born-Oppenheimer approximation. Due to the complex nature of interactions, time-dependent Schrödinger equation for a system with more than one atom can be solved with only fewer than 15 electrons[29]. Hence, Quantum Mechanical simulations are used to exploit some simplified models of interactions between electrons [30]. Well-known software packages such as AMPAC, VESP, CPMD, GAMESS, Q-Chem based on Density Functional Theory are used to study the nanoscopic (quantum) scale. As an example, structure of large molecules such as hexadecapeptide (with 80 heavy atoms) can be studied between a 1-5 days on a single 2 MHz Opteron processor.

3.2.2 Microscale

Simulations at the atomistic or microscopic scale of molecules are much more different than those at the quantum scale. A wide range of properties from thermodynamics to bulk transport characteristics of solids and liquids can be simulated. The typical timescale associated with this scale ranges from 10^{-12}s to 10^{-6}s for the longest runs on fastest supercomputers. Behaviors of the application systems in the microscopic scale are determined by their energy while the motion of their electrons is neglected. Individual atoms are described using "classical" interaction potentials and are governed by Newton's laws of motion. Difference in models is due to the method used in calculation of forces due to chemical bonds, hydrogen bonding, electrostatic, dipole-dipole and van der Waals interactions. Many different force fields [31] are suggested and mostly represent a trade-off between accuracy and numerical controllability. MD and Monte Carlo (MC) methods used for this scale are the two oldest methods on classical force fields. Bending, torsion and

coulomb interactions between molecules are only effective interactions and the quantum mechanical electronic contributions are neglected. Lennard-Jones (LJ) potential is a popular model potential in this scale and is known for its simplicity and numerical efficiency. Several academic software packages are available to use for free on this scale such as CHARMM, DL_POLY, GROMACS, IMD, and XMD or through commercial licenses such as GROMOS. In MD simulations, computational viability becomes an issue for even relatively small systems. As an example, simulations of pure lipids at the length scale of 10-30 nm and timescale of hundreds of nanoseconds are feasible. If a patch of lipid bilayer surrounded by water and ions with tens of thousands of particles needs to be simulated, the simulation of 1ns physics takes 1 to 2 days [32].

3.2.3 Mesoscale

If the application system has large number of atoms and need to be simulated for a long amount of time, the numerical viability of using an atomic model becomes an issue. Many real systems have large structures that cannot be studied at purely atomistic/microscopic scales. The typical timescale of simulation ranges from 10^{-8}s to 10^{-4}s. For example, soft matter systems, polymers, colloidal systems, cells and membranes fall under this category. In cells or membranes, self-organization of matter occurs and largely depends on interplay between their energy and entropy. However, by treating a cluster of atoms as one particle, the number of degrees in the system can be reduced. Such a process of 'coarse-graining' allows for running simulations much longer, extending the timescale to microseconds or even seconds, but at a loss of accuracy. These methods lie in the middle ground between MD and continuum approaches. The common idea behind the mesoscale simulation is to "average-out" the irrelevant microscopic details in order to

achieve computational efficiency and incorporating the essential features of the microscopic physics on the length scales of interest. Particle-based methods on this scale use variations of MD and MC methods and, as in the atomistic/microscopic scale, Newton's law of motion govern the behavior of the system. Examples of particle-based methods include DPD, Discrete Element Method (DEM) and CGMD. The Lattice-Boltzmann Method (LBM) is used to simulate fluids, where the system is solved using Navier-Stokes equation and the volume element of fluid is considered to be composed of collection of particles. The "bead-spring" model connects particles by flexible, entropic springs and is popularly used for studying polymer physics. As mesoscopic model couples between microscopic and continuum scales. Examples of solving problem at this scale include Finite Element Methods (FEM), Mean Field Theory (MFT) and Smooth Particle Hydrodynamics (SPH).

3.2.4 Macroscale

If the number of particles present in an application system becomes sufficiently large and the averaging of many degrees of freedom is done, one arrives at a single *continuum*. Rather than keeping track of individual particles, the flux of various systems can be calculated using diffusion and convection and modeled using partial differential equations (PDEs) and spatially varying density functions. The visco-elastic behavior and fluid properties are described using Navier-Stokes Equation. Computational Fluid Dynamics (CFD) is a popular technique used for finding the solution of the PDEs. Many commercial codes implementing the continuum theory-based methods are available for structural and coupled fluid-structural simulations in engineering

applications. Table 3.1 presents a short overview of the hierarchy of length scales common in typical applications and the typical simulation methods used for such scales.

Scale(m)	Typical Simulation Methods	Typical Applications
Nanoscale $\sim 10^{-12} - 10^{-9}$	Self-Consistent DFT (SC-DFT) Car-Parinello Molecular Dynamics (CPMD) (ab-initio) Quantum Monte Carlo (QMC)	Molecular geometry Electronic properties Entropy, Enthalpy Chemical reactions Dipole moments
Nanoscale/Microscale $\sim 10^{-9} - 10^{-6}$	MD and MC using classical fields Hybrid MD/MC Particle in Cell(PIC)	Equation of state Bulk transport properties Viscosity Rheology of fluids Polymers Biomaterials DNA models
Microscale/Mesoscale $\sim 10^{-8} - 10^{-1}$ $\sim 10^{-9} - 10^{-3}$ $\sim 10^{-9} - 10^{-4}$ $\sim 10^{-6} - 10^{2}$ $\sim 10^{-6} - 10^{2}$ $\sim 10^{-9} - 10^{-4}$ $\sim 10^{-6} - 10^{0}$	CGMD and MC using effective force fields DPD MFT FEM with microstructure included SPH LBM DEM	Complex fluids Soft matter Cell dynamics Phase transformations Diffusion Interface motion Granular matter Grain growth
Mesoscale/Macroscale $\sim 10^{-3} - 10^{2}$ $\sim 10^{-6} - 10^{2}$	CFD FEM,SPH, Finite Different Methods (FDM)	Macroscopic flow Macroscopic elasticity

Table 3.1: Classification of length scales and simulation methods in applications.

3.3 CGMD

MD methods are coveted for studying applications, but are often plagued by several limitations. For example, during computer simulation, the typical MD simulation produces astronomical data sets to analyze. The smallest useful dataset to be stored during simulation of one MD timestep is the 3D position coordinates (x, y, and z). With double precision of 8 bytes per coordinate, 24 Gigabytes of data needs to be stored for a one billion particle system in order to restart the system with old system coordinates. Besides particle coordinates-velocities, potential and kinetic energies need to be stored at each time step, resulting in >80GB for a billion particle system. Thus sophisticated software tools are required for on-the-fly analysis and are a challenge on current systems with Terabytes of hard-disk capabilities. Further, physical limitations are imposed by the atomic oscillations that are typically in the order of 10^{14} Hz. In order to evolve the system correctly, one timestep in an MD simulation should be in the order of femtoseconds (~10^{-15}s). Even with the largest length and time scales for atomic systems, a typical MD simulation run for millions of timesteps can only represent at most few hundred nanometers and few hundred nanoseconds, shorter than the biologically relevant molecular events. This bottleneck cannot be resolved with the availability of more number of processors as the time domain cannot be decomposed and distributed over CPUs as it can be done in spatial domain.

Thus CGMD is used as alternative by omitting irrelevant degrees of freedom in a system and simplifying the model. CG force fields have a wide range of resolutions (the number of atoms mapped onto one CG particle) and accordingly very different methods are used to construct the potential energy function. An extensive compilation of different methods, force fields and

application is give in [33]. Broadly speaking, there are three types by which to obtain CG potential: those that are entirely based on atomistic force field, entirely independent of any atomistic force field and a combination of two. The first type consist of methods like Boltzmann [34] and force matching [35, 36], where both the bonded and non-bonded terms are derived from atomistic simulations. The second type includes force fields that are parameterized purely by matching macroscopic properties of the system to experimental quantities [37, 38]. Examples include membrane bilayer properties or protein packing data derived from Protein Data Bank. Methods of the third type typically derive non-bonded interactions from experimental quantities (*e.g.* liquid properties) while partially relying on atomistic simulations for bonded interactions. Martini force field [39] is a popular technique that is used in this category.

The most expensive aspect of simulations is computation of the force term and must be determined at least once per temporal integration step. Thus by imposing kinematic constraints and eliminating high frequency axial vibrations of a system, we can reduce the cost of computing the force term. The averaging over detailed, local degrees of freedom leads to a smoother potential energy surface and consequently faster dynamics of CG models. Also it provides a significant increase in the stable temporal integrations step size and does not compromise on the fidelity of the model in representing the key behavior. The CG model considered in this thesis is loosely based on the "bead-spring" model for defining the platelet structure, where particles are connected through springs, and cannot cross over each other due to excluded volume, and have a certain stiffness defined by the bonded and angular potentials. The non-bonded interactions are defined by the LJ potential owing to their simplicity and numerical efficiency.

DPD introduced by Hoogerbrugge and Koelman in 1992 is another such discrete particle simulation methodology in which the length scale ranges from 10^{-9} – 10^{-3} m and were able to simulate the dynamics of isothermal fluids. DPD combines the benefits of MD and Lattice-Gas Automata simulations. DPD can represent a fluid with a collection of particles with prescribed conservative dissipative and stochastic interactions that conserve momentum and produce hydrodynamic behavior. One limitation of DPD is that the transport coefficients cannot be directly related to macroscopic parameters and need to been done through kinetic energy [40, 41].

The algorithm of CGMD and DPD simulations is similar to MD simulations and broadly contains five steps:

1) **Initialize** - Read initial states of the particles.
2) **Ensembles and Interaction** - Calculate the forces acting on each particle based on neighbor list.
3) **Force Calculations** - Compute the acceleration of each particle.
4) **Integration** - Obtain the velocities and positions of the particles after each time step.
5) **Analyze** - Compute magnitudes of interest and measure observables. Repeat steps 2 through 5 for the required number of time-steps.

Note that CGMD and DPD are identical to MD in spirit but the physics is fundamentally different. However, for modeling the particle properties, force interactions and integration laws that are classified as MD techniques are also used in CGMD and DPD to understand the collective behavior of large-particle system. These techniques are briefly discussed below.

3.3.1 Force Calculations and Ensembles

Particles in the CGMD and DPD systems move due to the forces acting on them and are governed by Newton's second law of motion:

$$\vec{F} = m\vec{a} = m\frac{d\vec{v}}{dt} = m\frac{d^2\vec{r}}{dt^2} \quad 3.1$$

The potential energy between the individual particles helps in determining the atomic interactions, described by inter-atomic forces between particles. The sum of the potential energy associated with all types of atomic interactions gives the total potential energy (U) of the system. The forces acting between the pair of particles (i, j) are computed by evaluating the negative first order derivative of total potential energy with respect to the separation distance.

$$\vec{F} = -\frac{\partial U}{\partial r_{ij}} \quad 3.2$$

The sampling during simulations is conditioned on the ergodicity principle: the properties of a system are the same when averaged over time as averaged over many systems. The set of all states of the system is called an "ensemble". Depending on which constraints are applied to the system different ensembles can be obtained. Some examples are the microcanonical ensemble (with the particle number (N), system volume (V) and total energy (E) imposed), the canonical ensemble (with N, V and system temperature (T) imposed) and the Gibb's ensemble (with N, system pressure (P) and T imposed) [42]. NVE microcanonical ensemble is used in this thesis.

The ergodicity principle also infers that for a system in equilibrium, running one long simulation is the same result as running multiple short simulations. This principle allows us to

perform multiple simulations in parallel on different computers. However, it also assumes that the separate systems are in equilibrium, which for some processes might not be feasible in short simulations because the required long processes of equilibrations. For these cases most software packages have implemented parallelization schemes [43] that allow a single simulation to run on multiple processors, by distributing the calculations. In this way longer simulations of larger systems can be simulated in the same time by using very large computers.

3.3.2 Integration

A variety of different numerical methods are available for integrating the equations of motion [44]. As force evaluation is the most intensive part of the computation, an integration method that can do at most one calculation per timestep or can provide sufficient accuracy with increase in the size of the timestep Δt for more calculations per timestep is desirable. Due to the strong repulsive forces of a typical LJ-based potential at short distances, there is an upper bound on the Δt and even the well-known Runga-Kutta Methods are unable to enlarge the timestep beyond this limit. However obtaining a high degree of accuracy in trajectories is neither a realistic or practical goal. This can be attributed to the sharply repulsive potentials resulting in trajectories that are extremely sensitive to numerical errors (almost exponential) superseding the local truncation errors (power-law) introduced by most of the numerical integrators and even the round off errors. Also the trajectory accuracy beyond several averaged ‘collision times’ is not as meaningful. Hence, it is desirable to have numerical methods that can provide energy conservation and reproduce time and space-dependent correlations with a certain degree of accuracy.

Popular integration methods are Verlet, leapfrog, Velocity-Verlet and Beeman's algorithm. The simulation software packages used in this thesis use the Velocity-Verlet (a variant of Verlet) integration scheme and is discussed below. The essence of this algorithm is to calculate the positions of particles after every time step from current positions. The Verlet algorithm can be derived from Taylor expansions, one forward and one backward in time:

$$r(t + \Delta t) = r(t) + \dot{r}(t)\Delta t + \frac{1}{2}\ddot{r}(t)\Delta t^2 + \frac{1}{6}\dddot{r}(t)\Delta t^3 + O(\Delta t^4) \quad 3.3$$

$$r(t - \Delta t) = r(t) - \dot{r}(t)\Delta t + \frac{1}{2}\ddot{r}(t)\Delta t^2 - \frac{1}{6}\dddot{r}(t)\Delta t^3 + O(\Delta t^4) \quad 3.4$$

where $\dot{r}(t) = v(t)$ is the velocity and $\ddot{r}(t) = a(t)$ is the acceleration of a particle at time t. Adding equations 3.3and 3.4 we get,

$$r(t + \Delta t) = 2r(t) - r(t - \Delta t) + \ddot{r}(t)\Delta t^2 + O(\Delta t^4) \quad 3.5$$

which is the position one step after time t and the position is expressed as a function of current position, the previous time-step position and acceleration. The truncation error is of the order Δt^4. At the very first time step, the previous position r(t-Δt) is not defined for the basic Verlet algorithm. Velocity-Verlet algorithm fixes this issue by calculating the velocity and position at the same time step (derivation not shown) as follows:

$$r(t + \Delta t) = r(t) + v(t)\Delta t + \frac{1}{2}a(t)\Delta t^2 \quad 3.6$$

$$v(t + \Delta t) = v(t) + \left(\frac{a(t) + a(t + \Delta t)}{2}\right)\Delta t \quad 3.7$$

where $a(t) = \frac{F(x(t))}{m}$.

The steps for Velocity-Verlet algorithm are as follows:

Step 1: Calculate $r(t + \Delta t) = r(t) + v(t)\Delta t + \frac{F(x(t))}{2m}\Delta t^2$

Step 2: Calculate $F(x(t + \Delta t))$

Step 3: Calculate $v(t + \Delta t) = v(t) + \frac{\Delta t}{2m}\left(F\left(x(t + \Delta t)\right) + F\left(x(t)\right)\right)$

3.3.3 Periodic Boundary Condition and Neighbor List

All simulations take place in a bounding box or a container of some shape and size. If one needs to model much larger realistic systems at the microscopic level with finite means, periodic boundary condition (PBC) is usually adopted. PBC is achieved by treating an infinite array of identical copies of the simulation region in all dimensions (Figure 3.3). There are two implications to the PBC approach. First, a particle leaving the simulation region through a particular bounding face of the simulation region reenters the region through the opposite face. Second, particles that are within a distance r_c distance of a bounding face interact with particles within the same distance near the opposite bounding face, effectively creating a wraparound phenomenon. These two considerations are taken into account while calculating the forces and integrating the position and velocities of particles.

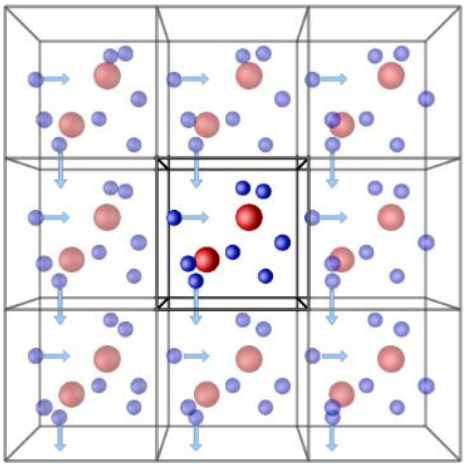

Figure 3.3: Periodic boundary conditions in 3D for a simulation region. Particle leaving the lower bounding face enters the simulation region through the upper bounding face. (Source: http://isaacs.sourceforge.net/phys/pbc.html)

Each particle in the simulation typically needs to interact with all other particle in a simulation step, which leads to a total of $O(n^2)$ force calculations per step. To tackle this huge computation load, simulation softwares employ a neighbor list strategy to calculate the interactions with the approximation of truncating interactions from particles at a cut off radius r_{cut} away, practically limiting the number of interactions for each particle. A drawback of this method is that the neighbor list requires frequent updates for every time step and thus consumes a considerable amount of time. This added cost of updating the list is reduced, by introducing a buffer radius r_b to the cutoff radius r_{cut} to get a neighbor list radius r_s (Figure 3.4). This r_b helps in displacement of particles beyond r_{cut} but still within the r_s thereby reducing the number of times the neighbor list is updated. Although this requires additional memory of O(n), it is affordable as it reduces the computation to O(n) as compared to $O(n^2)$ for large number of particles.

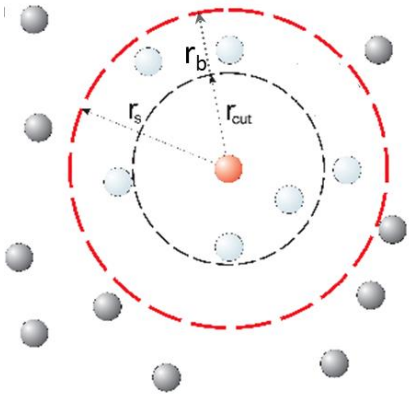

Figure 3.4: Interactions of a particle (shown in red) in a system using the neighbor list.

3.4 Simulation Packages

Simulations in this thesis are performed using the open source software packages NAMD, Not (just) Another Molecular Dynamics program, and LAMMPS, Large-scale Atomic/Molecular Massively Parallel Simulator. Overview of these packages are discussed here.

NAMD

NAMD [45] is a parallel MD code developed at the University of Illinois at Urbana-Champaign, as a collaborative project involving the Theoretical and Computational Biophysics Group (http://www.ks.uiuc.edu) and the Computer Science Department, including the Parallel Programming Laboratory (http://charm.cs.uiuc.edu). NAMD uses an effective parallelization strategy that is a hybrid of spatial decomposition and force decomposition. This is supported further by dynamic load balancing capabilities [46] of the Charm++ parallel programming system. This hybrid parallelization strategy has remained effective over the past ten years. In any MD simulation, calculation of the non-bonded forces between all pairs of atoms is the most

computationally demanding with a time complexity of $O(n^2)$. In order to reduce time complexity of this algorithm to O(nlogn), the terms cutoff radius r_{cut}, that separates the computation of short-range forces and long-range forces were introduced [46]. For the atoms within the cutoff radius r_{cut} non-bonded forces are calculated on per atom basis. For the atoms outside the r_{cut}, long-range forces are calculated using particle-mesh Ewald algorithm, which has a O(nlogn) time complexity. Decomposition of computation in this way, results in calculation of non-bonded forces for atoms within the r_{cut} being responsible for 90% of total computational effort. NAMD is used to simulate the single platelet in vacuum and parameterize the CGMD system.

LAMMPS

LAMMPS [47] is a versatile, parallel, highly optimized, open source code for performing MD and DPD simulations of CG models. It is written in C++ and uses integration of Newton's equation of motion for a system of interacting particles via short or long range forces. LAMMPS has a good Message Passing Interface (MPI) interface and scales well with large number of processors; its speedup generally increases with the increase in the number of atoms used in the simulation. Also GPU acceleration is possible in LAMMPS. LAMMPS has the STUBS library that acts like a wrapper for the MPI library and hence can also be run on a single processor. LAMMPS used the spatial decomposition technique to decompose the simulation region into small sub-domains and assigning a processor to each such domain. A wide variety of constraints including statistical ensembles, thermostats, forces and springs are implemented. Computations are done as time averaged measurement a discussed in Section 3.4. These computations include measurements of pressure, temperature, potential energy and other thermodynamic properties.

NAMD and LAMMPS generate output data that can be visualized in a separate software called Visual Molecular Dynamics (VMD) [48]. VMD can be used to debug any problems with the input scripts and generate snapshots of the simulations. Most of the images in Chapter 4 are generated using VMD.

3.5 Supercomputer Platforms

An evolutional view of supercomputers and the latest ones that are relevant to my research are discussed below.

3.5.1 Supercomputers

The origin of the computer simulations on supercomputers can be traced back to the first programmable computer Z3 in early 1930s in Germany. However, a more well-known equivalent is the American Electronic Numerical Integrator and Computer (ENIAC) developed in 1946 during World War 2 at the Los Alamos Laboratories and was used to study thermonuclear reactions, by calculating their ballistic curves and hydrodynamics of shock waves. ENIAC (Figure 3.5) is considered to be the *first-generation* of electronic computers that weighs more than 30 tons and contained 18,000 vacuum tubes and was 1000 times faster than their electro-mechanical competitors. It was connected by plugging cables and wires and setting switches that spanned over the whole system. ENIAC's clock speed was 100 KHz while traditional PCs today has a clock speed of 3.2GHz. The first problem run on ENIAC was to check the feasibility of the hydrogen

bomb, and it took 20 seconds to process half a million punch cards that were prepared for about six weeks.

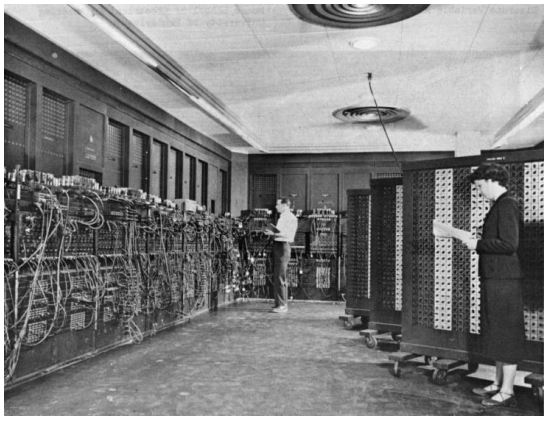

Figure 3.5: The first modern supercomputer ENIAC with cables and programming panels can be seen at the left and the 3000 switches for the function tables at right. (U.S. Army photo)

With the introduction of "von Neumann principles" [49], the program which was represented by the excessive physical modification of switches and cords, was now also represented electronically like the data. This led to the invention of Mathematical Analyzer, Integrator and Computer (MANIAC) from 1948-1952 in Los Alamos Laboratories. The programming was of the lowest level, machine language, and the data cells were addressed and shifted around directly in the memory. With the accessibility of electronic computers by 1950s for everyday use, the field of *scientific computing* was shaped. The first problems were solved by E. Fermi et.al for phase shift analysis of pion-proton scattering [50] and G. Gamow for genetic coding [51]. One of the first N-body problems was done on the MANIAC to study the equation of state in two dimensions for a system of rigid spheres [52] using the MC Method [53]. In 1956, the first ever MD simulation was conducted on UNIVAC (first commercial computer) and used to calculate the velocity auto-correlation function and self-diffusion coefficient for a system with N=256 hard

spheres with periodic boundary conditions [54]. As a comparison, approximately $N \sim 10^5$ particles with simple hard sphere MD simulations can be run on a current generation PC. In 1964, A "real" fluid was simulated under MD principles by 864 LJ particles of fluid Argon [55].

The *second-generation* of computers were developed in all aspects of design, from the hardware composed of basic circuits (discrete diodes and transistors with switching time ~0.3 seconds) to software programming languages used to write scientific applications. Many high level languages were introduced, like FORTRAN (1956), ALGOL (1958) and COBOL (1959). The first two supercomputers, Livermore Atomic Research Computer and IBM 7030(Stretch) were used to do numerical processing in scientific applications.

The *third-generation* came with major innovations in integrated circuits with many transistors on chip, semiconductor memories and microprogramming for designing complex processors, pipelining, parallel processing, birth of operating systems and timesharing. Particularly, C programming [56] and C-based UNIX operating system were vital in this generation. The UNIX was ported on many different kinds of computers, relieving the user from learning each new operating system, and now, is the standard operating system on all computer systems that are used for scientific high-performance computing. Seymour Cray also developed CDC 6600, the first of its kind to use functional parallelism for its architecture. CDC 6600 comprised of 32 independent memory banks and 10 functional units, and was able to perform at 1 Millionflops.

The *fourth-generation* came with large scale integration with 1000 devices per chip and very large scale integration (100,000 devices per chip) in computer systems. Entire computers (processors, main memory and I/O controllers) could be fit on to a chip and gate delays dropped

to about 1ns per gate. Semiconductor memories previously just used for registers and caches were now used for main memories. High-speed vector processors suck as CRAY 1, and CRAY X-MP (Figure 3.6) were used in HPC. Parallel architectures were developed majorly and experimental parallel computing efforts were done.

Figure 3.6: The Cray X-MP with processors stacks in circular arrangement, typical of Cray machines. It was capable of performing 800 Megaflops

The *fifth generation* came with introduction of machines with hundreds of processors that could work on different parts of a single application, a major leap from the previously established parallelism in the form of pipelining and vector processing. A popular computing system "hypercube", the Intel iPSC-1, gave each processor its own memory and a network interface to connect all processors. With this distributed memory architecture, memory access by many processors was no longer a bottleneck and larger systems with more processors could be built. With the introduction of computer networking, local area network (LAN) and wide area network (WAN) a distributed computing environment was possible, where the users could use their work-stations for editing files but share expensive resources such as file servers and supercomputers. The quality and quantity of scientific visualization also was improved during this time.

The five generations lasting till 1990s would define the base for the future developments in supercomputing technology and applications. Any advancement in hardware or software from 1990s was gradual. In fact, since 1983, twice a year, a list of the 500 most powerful computing systems is studied, recorded and released on a popular website, Top500.org [57]. Linpack benchmark [58] is used for measuring the performance and ranking these supercomputer systems. Table 3.2 lists the latest top 10 supercomputers released on November 2014 according to the Linpack performance measured in Teraflops (Tflops).

Rank	**Name, Location**	**System Model**	**Linpack Performance Rmax (Tflops)**	**Efficiency (%) (Rmax/Rpeak)**	**Cores**	**Processor Model**	**Interconnect**
1	Tianhe-2, China	TH-IVB-FEP Cluster	33862.7	61.68	3120000	Intel Xeon E5-2692v2 12C 2.2GHz	Custom Interconnect
2	Titan, U.S.	Cray XK7	17590.0	64.88	560640	Opteron 6274 16C 2.2GHz	Cray Gemini Interconnect
3	Sequoia, Japan	BlueGene/Q	17173.2	85.30	1572864	Power BQC 16C 1.6GHz	Custom Interconnect
4	K computer, U.S.	K computer	10,510.0	93.17	705024	SPARC64 VIIIfx 8C 2GHz	Custom Interconnect
5	Mira, U.S.	BlueGene/Q	8586.6	85.30	786432	Power BQC 16C 1.6GHz	Custom Interconnect
6	Piz Daint, Switzerland	Cray XC30	6271.0	80.51	115984	Xeon E5-2670 8C 2.6GHz	Cray Aries Custom Interconnect
7	Stampede, U.S.	PowerEdge C8220	5168.1	60.66	462462	Xeon E5-2680 8C 2.7GHz	Infiniband FDR
8	JUQUEEN, Germany	BlueGene/Q	5008.9	85.30	458752	Power BQC 16C 1.6GHz	Custom Interconnect
9	Vulcan, U.S.	BlueGene/Q	4293.3	85.30	393216	Power BQC 16C 1.6GHz	Custom Interconnect
10	Cray CS-Storm, U.S.	Cray CS-Storm	3577.0	58.33	72800	Intel Xeon E5-2660v2 10C 2.2GHz	Infiniband FDR

Table 3.2: Top 10 supercomputer list as of November 2014.

3.5.2 Our Platforms

In this thesis, the majority of the simulations were conducted on the Sunway Blue Light System and the Beowulf cluster using Intel processors and Mellanox Infiniband network switches at the National Supercomputer Center in Jinan, China. Some of the initial simulations used for model parameterization were done using the BlueGene/L system at the Brookhaven National Laboratory, Upton, New York. Given below is a brief overview of the three systems.

The Sunway Blue Light system is a massive parallel processing (MPP) computer, which uses Chinese-made processors. It is one of three Petaflop-level supercomputers in China in 2011; the other two are Tianhe-1A in Tianjin and Nebulae in Shenzhen. The system has integrated 8,704 ShenWei SW1600 16-Core processors at clock speeds varying from 975 MHz to 1200 MHz, and each of these processors has 128 GigaFlops of peak performance and up to 16 GB of memory. Its interconnection subsystem is built by the Infiniband QDR switched network providing 40 Gbps (Gigabits per second) per link connection. Operating 8,575 CPUs at 975 MHz, it ranked No. 2 in the 2011 release of China HPC Top100 and No. 14 in the 2011 November release of Top500 list.

The Beowulf Cluster that's locally called "the Intel machine" in Jinan has a total of 700 blade nodes each consisting of 2 Intel Xeon X5675 6-core Processors. The CPU frequency is 3.06GHz. One processor delivers a total performance of 73.584 Gigaflops. Two CPUs are set in each node; therefore, the peak theoretical performance of a single node is 73,584 × 2 = 147.168 GigaFlops, On-chip memory is 36GB DDR3 RDIMM and are also equipped with 1 InfiniBand QDR HCA card and 2 1000Mbps (Megabits per second) Ethernet Adapter.

New York Blue is an 18-rack IBM BlueGene/L massively parallel supercomputer. Each of the 18 racks consists of 1024 compute nodes (a total of 18432 nodes) with each node containing two 700 MHz PowerPC 440 core processors and 1 GB of memory (a total of 36864 processors and 18.4 TB of memory). The racks are arranged as six rows of three racks each. With a peak performance of 103.22 Tflops, New York Blue allows computations critical for research in biology, medicine, material science, nanoscience, renewable energy, climate science, finance and technology.

Chapter 4

Single Platelet Model in Vacuum

The applications of the simulation techniques covered in preceding chapters that contribute to the whole–cell modeling of a platelet are presented. It is infeasible to consider all the bio-cellular reactions that occur in a cell at this state of computer speeds, but rather focused on designing a simulation system that can collectively encompass the mechanical behavior of a platelet. First the platelet model used for the cellular description of a platelet structure is described. The mechanical model enables the description of resting platelets and the controllable simulation of activated platelets by developing filopodia, as observed in experiments. Each of these components in the model is designed to mimic the physiological geometry of the platelet and its corresponding biomechanical properties.

4.1 Challenges of Numerical Modeling

Numerical modeling of the platelet activation processes caused by mechanical stimuli is a major challenge. The non-spherical discoid shape characterizing platelets' initial morphology and the ensuing rapid shape change during activation by extrusion of filopodia requires a platelet model that is capable of depicting such dynamic deformable behavior. Describing the rheological blood flow at the macroscale level, some investigators considered platelets as particles and showed the strong effect of fluid stresses [59, 60] and fluid flows [61] on platelet aggregation. At the cellular

level, several studies incorporating platelets' role in response to biomechanical processes have been conducted. In order to understand their hydrodynamics and aggregate dynamics, platelets were first treated as smooth solid spheres [62, 63]. Later, numerical studies were conducted to analyze the sedimentation behavior as a function of distance from the wall, where the platelets were treated as hexagonal flakes [64]. In other studies, platelets were treated analytically as thin 2D elliptical planar surfaces to understand the mechanics of the tethering process as they flip on a surface [65] and lateral motion near wall induced by RBCs [66]. Platelets were further modeled as 3D oblate spheroid [67] of aspect ratio 0.25 to study flipping of an adhesive platelet over a substrate. Similar 3D oblate spheroids [68, 69] were used to characterize the adhesion of colliding platelet surfaces near wall. In 2011, a 3D CG rigid oblate spheroid flow-cell interaction model [70] was developed using sub-cellular elements to simulate cell motion, with the cell coupled to the plasma flow by the Langevin equation. These modeling approaches advanced the simulations of biomechanical processes such as platelet flipping and adhering, but excluded more complicated morphological changes such as filopodia formation which play an essential role in platelet aggregation and adhesion.

Platelet pseudopodia, particularly filopodia - the long, finger-like projections, have been observed to play a role in both aggregation and adhesion. Aggregation efficiency improves due to both filopod number and length [71], possibly due to localization of the GPIIb-IIIa receptors on them, which allow the platelets to stick to each other [72]. Furthermore, filopods on platelets have been shown to support rolling on a thrombogenic surface under high shear flow [73]. Recently, pseudopodia growth on platelets under static adhesion has been examined using imaging

techniques [74-76], but their dynamic growth on platelets due to shear-induced activation has not been observed.

An atomic scale-based model can describe such formation, but requires trillions of atoms for modeling a single platelet and complicated molecular force field formulations that exceeds current computing capability [77]. A CGMD approach is computationally feasible and more efficient for analyzing the complex dynamics observed during platelet activation. In the CGMD method, a collection of atoms or molecules is considered as one representative particle, allowing the simulation of larger systems with longer simulation time [78]. CGMD is especially useful for phenomena occurring at different scales, for *e.g.*, the mechanical processes governing the cell and its internal structures occurring at the order of nano, micro, milli, to even few seconds.

Recently, CGMD has been used to study and simulate the mechanical behavior of actin cytoskeleton which aides in cell morphology and movement and spans the spatial-temporal scales [79]. Advancing from the traditional continuum approaches, a phenomenological CGMD model comprising of discrete particles interacting with CGMD force fields is developed in this study. By considering the principal intra-platelet constituents, this computationally affordable 3D model is capable of emulating a platelet in its quiescent state. This model, while not directly representing the platelet physiology, can simulate the dynamic process of filopodia formation. This filopodia formation is a key observation during early stage platelet activation [80] when platelets are exposed to varying levels of fluid shear stresses. The cell geometry, filopodia length and thickness can be modeled by directly correlating nanoscopic model parameters to experimental measurements.

4.2 Quantitative Description of a Platelet

In its quiescent state, the discoid platelet (Figure 4.1a) is composed of three zones: the peripheral, structural and organelle as discussed in Section 2.1. The peripheral zone can stretch and deform during filopodia formation. The structural zone has a cytoskeletal assembly with two key components, an actin-based filament network and a spectrin-based membrane skeleton. During the initial stages of activation, actin-based filament network reassembles and polymerizes, deforming the membrane to form filopodia. The organelle zone is responsible for metabolic events of the platelet but its mechanical role in growth of filopodia is negligible.

In order to simulate the shape change of the platelet before and during the formation of filopodia, phenomenological functions of each zone is characterized. Accordingly, the platelet model consists of three main components: the membrane, cytoskeletal assembly and cytoplasm (Figure 4.1b). The membrane (thickness of 300A) is designed as a cortical shell for representing the stretchable peripheral zone that includes the phospholipid bilayer and the exterior coat. Following the works in [81-86], the membrane is, characterized by spring-connected particles (Figure 4.1c) residing at the nodes of a network of triangles constructed by the 3D Delaunay triangulation method [87]. The surface invaginations caused by the OCS that account for the extra membrane, are represented to a certain degree by this stretchable membrane allowing it to be intact during filopodia formation.

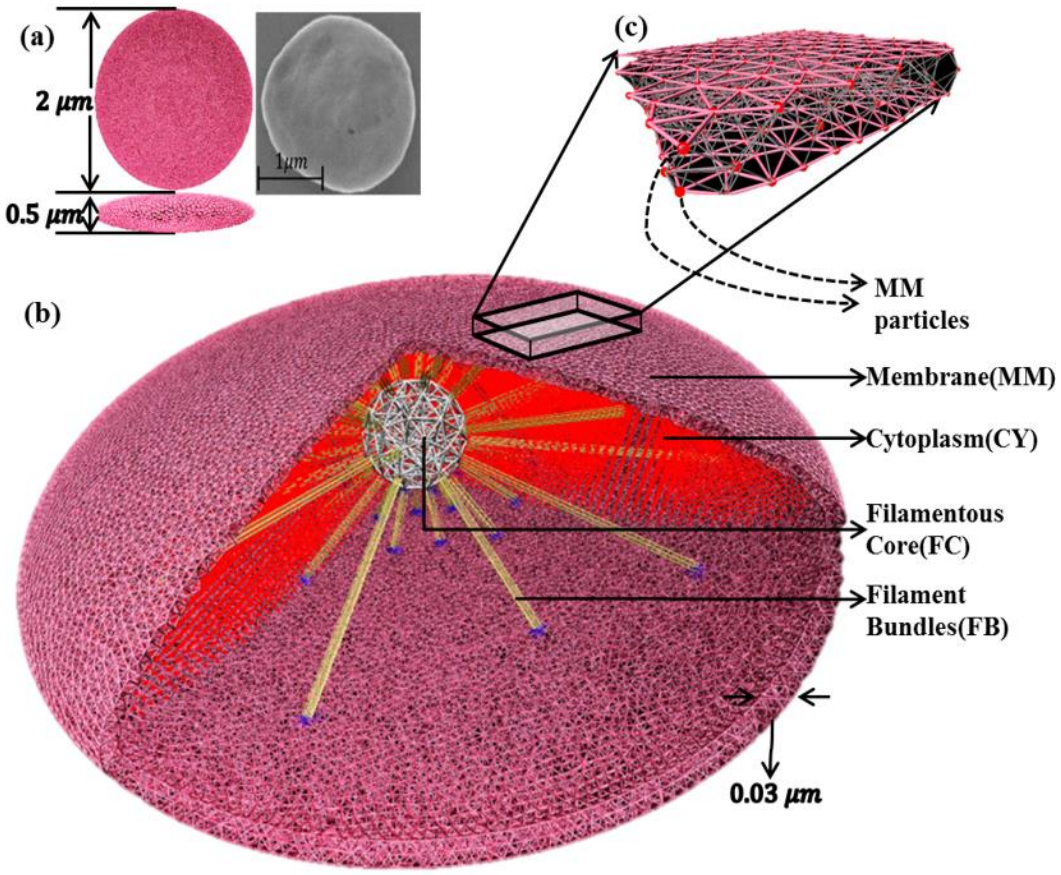

Figure 4.1: 3D model geometry of the simulated platelet. (a) The orthographic view of the platelet model in comparison to the experimental Scanning Electron Microscopy (SEM) image of the quiescent platelet. (b) Model components representing the various zones of the phenomenological platelet: membrane, cytoskeletal assembly (filamentous core and filament bundles) and cytoplasm. (c) Membrane piece shown with particles connected with spring bonds. The membrane and cytoplasm particles constitute 80% of the total number of particles and play a major role in maintaining the discoid shape during quiescent state and deformation during formation of filopodia. The cytoskeletal assembly particles constitute rest of the 20% and their structural mechanics promote filopod formation.

The cytoskeletal assembly is designed for representing the actin-based structural zone. The spectrin-based membrane skeleton and the microtubule coil that disassemble after activation are

not included in the model. Also, microtubule dynamics is not involved prior to sphering of the platelet, a later stage in activation [13]. The actin cortex and radiating actin filaments functions of the structural zone are modeled by the rigid filamentous core and protrusible filament bundles respectively (Figure 4.1b) to resemble the spoke-like assembly. The filamentous core (Figure 4.2) is constructed by uniformly distributing spring-connected particles along the edges and vertices of a 3D triangulation of a sphere with diameter 0.3 μm. The rigidity of the core is ensured by both the global polyhedral stability and the local stiffness of the spring-connected particles.

Due to the experimental limitations in isolating and measuring the cytoskeletal assembly from platelets that are still relatively discoid (*i.e.* not highly activated or spread), an approximated diameter for the core is used. The filament bundles originating from the exterior of the filamentous core extend radially outward using spring-connected particles, and deform the platelet membrane to form filopodia. The filament bundles are treated as straight spring bundles before activation, and generate an extension-dependent force. Each filament bundle is connected to the membrane via a few spring bonds (Figure 4.2a) that mimic spectrin and adducin activity [15] on the actin filament ends. Actin-based filopodia formation, in reality, entails a hierarchical structure on multiple length (and time) scales and it is a combination of chemical interactions and mechanical feedbacks [88]. Polymerization of actin filaments occur near the cell's membrane pushing the membrane outward, forming the protrusion and driving the filopodia growth. In addition, many cross-linking proteins bundle the parallel actin filaments together, increasing their mechanical stability [89].

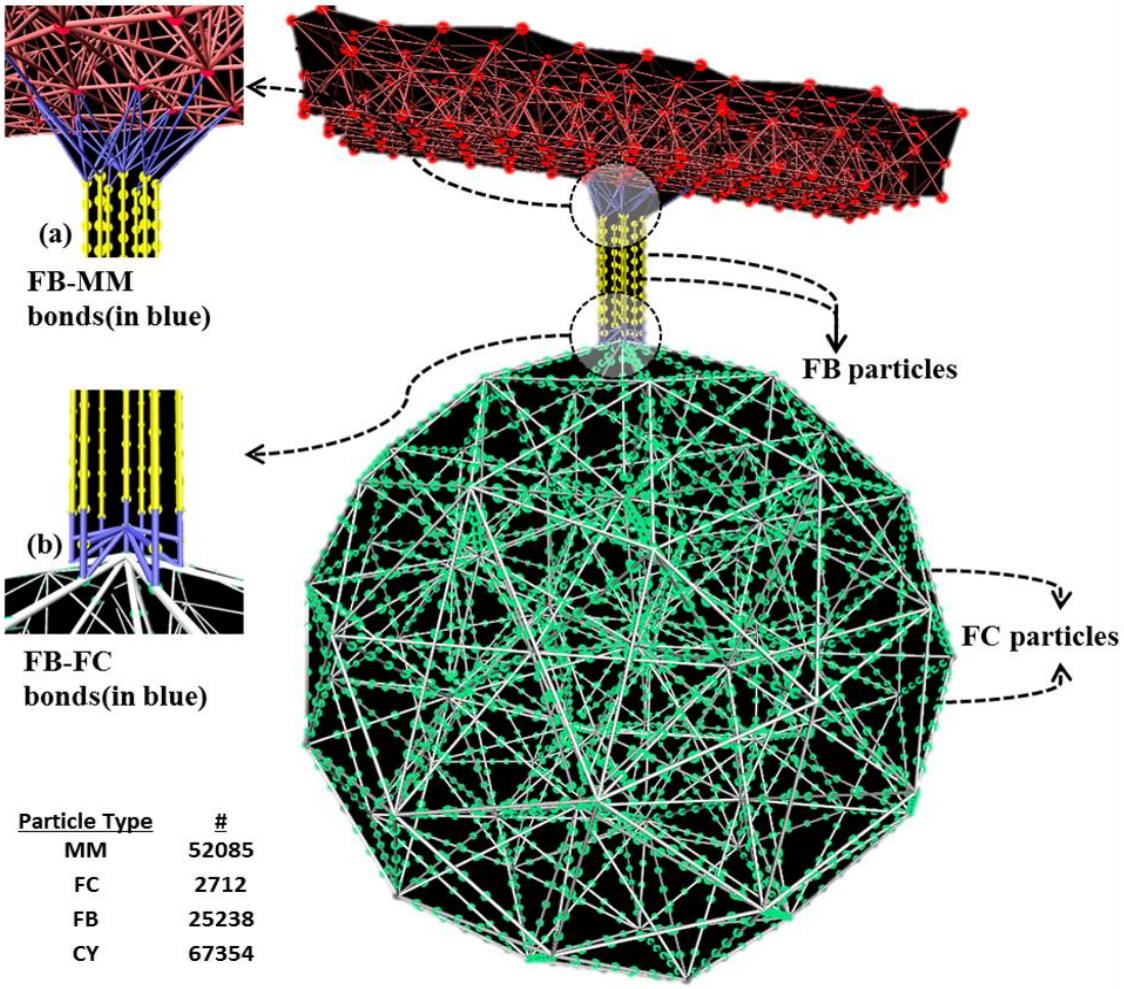

Figure 4.2: Filamentous core connected to the membrane via filament bundles which are all represented by spring-connected particles. (a) Spring bond between filament bundle (FB) particles and membrane (MM). (b) Spring bond between filamentous core (FC) and FB particles. The number of particles for individual model components is listed.

Stochastic simulations based on the atomistic mechano-chemical nature of actin polymerization dynamics were extensively studied [90-93]. Also, several researchers have studied the role of cross-linking proteins on material properties of actin filament [94, 95]. To consider all the atomistic details of the polymerization process leading to filopodia formation along with the

complete platelet structure although desirable, will impose restrictions on the computational domain size and simulation time scales [92]. Hence in this model, the filament bundles are coarse-grained as straight spring bundles before activation, and the spring bundles generate the classic spring force during filopodia formation. This numerical approximation of the filaments, while emulating the morphology at coarser scales than the atomistic scale, reflects the mechanical growth of filament bundles for forming filopodia. The cytoplasm [96] represents the inhomogeneous organelle zone and is characterized by a swarm of homogeneous particles that interact with each other through basic force laws. The cytoplasm particles are used to represent the gel-like behavior of the organelle zone and thus, help in preserving the shape of the platelet in quiescent state and during filopodia formation.

4.3 The Potential of Particles in a Platelet

A representative reduced molecular-scale force field [97] is used to describe the interaction between the particles of platelet model components. It includes the bonded (bonds and angles) and the non-bonded (LJ potential) interactions and is given by:

$$V = \sum_{\text{bonds}} V_B(r) + \sum_{\text{angles}} V_\theta(\theta) + \sum_{\substack{\text{nonbonded} \\ \text{pairs}}} U_{LJ}(r) \qquad 4.1$$

where, $V_B(r) = k_b(r - r_0)^2, V_\theta(\theta) = k_\theta(\theta - \theta_0)^2, U_{LJ}(r) = 4\epsilon\left[\left(\frac{\sigma}{r}\right)^{12} - \left(\frac{\sigma}{r}\right)^{6}\right]$. V is the total energy of a particle. $V_B(r)$ and $V_\theta(\theta)$ are the bond and angle potentials, k_b and k_θ are the spring and angle force constants, r_0 and θ_0 are the equilibrium distance and angle. $U_{LJ}(r)$ is the

nonbonded LJ potential, ϵ is the depth of the potential well and σ is the finite distance at which the inter-particle potential vanishes. r is the position of the particle in 3D and θ is the angle between three connected particles.

4.3.1 Filamentous Core

The bond energy between two adjacent filamentous core particles is given by:

$$V_B(r) = \frac{k_{fc}}{2}(r - r_{fc})^2$$

$$k_{fc} = 10^5 \text{ kcal mol}^{-1}\text{A}^{-2} \qquad 4.2$$

$$r_{fc} = 107.5 \text{ A}$$

where r_{fc} is the equilibrium distance between two adjacent filamentous core particles and its value is chosen to provide considerable computational speedup while retaining suitable fine discretization of the filamentous core network. k_{fc} is the spring force constant of two connected filamentous core particle and its value is chosen in order to achieve the increased rigidity in the filamentous core. As a result, filament bundles that rest on the filamentous core grow radially outward during filopodia formation, instead of pushing down on it. The angle energy of a triplet of filamentous core particles is given by:

$$V_A(\theta) = \frac{k_{fc\theta}}{2}(\theta - \theta_{fc})^2$$

$$k_{fc\theta} = 10^9 \text{ kcal mol}^{-1}\text{rad}^{-2} \qquad 4.3$$

$$\theta_{fc} = 180°$$

This high angular energy ensures the filamentous core rigidity and provides resistance to bending when the forces from the filament bundle's extension push down on it. $\epsilon_{fc} = 1$ kcal mol^{-1} is chosen to be similar to the cytoplasm ϵ_{cy} to keep the non-bonded interactions as uniform as possible. The $\sigma_{fc} = 190$ A value is chosen to limit the non-bonded interaction between filamentous core particles.

4.3.2 Filament Bundles

The bond energy between two adjacent filament bundle particles is given by:

$$V_B(r) = \frac{k_{fb}}{2}\left(r - r_{ts,fb}\right)^2 \qquad 4.4$$
$$k_{fb} = 50 \text{ kcal mol}^{-1}\text{A}^{-2}$$

where $r_{ts,fb}$ is a variable used to control the length of the filopod. The stiffness of actin filaments is in the range of 5.61 – 10.27 kcal mol^{-1}A^{-2} as reported in [98, 99]. $k_{fb} = 50$ kcal mol^{-1}A^{-2} ensures a stiffer filament bundle that is able to push the membrane during formation of filopodia. At timestep ts=0, $r_{0,fb} = 50$ A. The angle energy of a triplet of filament bundle particles is given by:

$$V_A(\theta) = \frac{k_{fb\theta}}{2}(\theta - \theta_{fb})^2 \qquad 4.5$$
$$k_{fb\theta} = 10^6 \text{ kcal mol}^{-1}\text{rad}^{-2}$$

$$\theta_{fb} = 180°$$

This angular energy ensures that the filament bundles have strong resistance to bending or buckling. The non-bonded interaction between the filament bundle and the membrane must have stronger repulsive forces so that the membrane can move and encompass the protruding filament bundle effectively. Hence, $\epsilon_{fb} = 1000$ kcal mol^{-1} is used to address this requirement [100]. $\sigma_{ts,fb}$ is a variable that is used to control the thickness of the filopod, where $\sigma_{0,fb} = 90$ A. In addition, following the previous works in [101-103], the excluded volume interaction between filament bundles is represented by the repulsive term in the non-bonded LJ potential

4.3.3 Membrane and Cytoplasm

The bond energy between two adjacent membrane particles is given by:

$$V_B(r) = \frac{k_{mm}}{2}(r - r_{mm})^2$$

$$k_{mm} = 0.00005 \text{ kcal mol}^{-1}\text{A}^{-2} \quad (4.6)$$

$$r_{mm} = 215 \text{ A}$$

where r_{mm} is the equilibrium distance between two membrane particles and is chosen to be 215A to describe a two-layer structure. It enables us to adapt the mechanobiological elasticity by adjusting the spring force constant k_{mm} between membrane particles. The area-stretching method is used to estimate the Young's modulus of the platelet membrane (simulations run on LAMMPS). The schematics of the experiment and the elastic response are illustrated in Figure 4.3. The Young's modulus of human platelets is $(1.7 \pm 0.6) \times 10^3$ dyne cm^{-2} as reported in Table 1 of

[104]. For the $k_{mm} = 0.00005$ kcal $mol^{-1}A^{-2}$, the Young's modulus of the particle-based CGMD platelet model is $(1.46 \pm 0.02) \times 10^3$ dyne cm^{-2}.

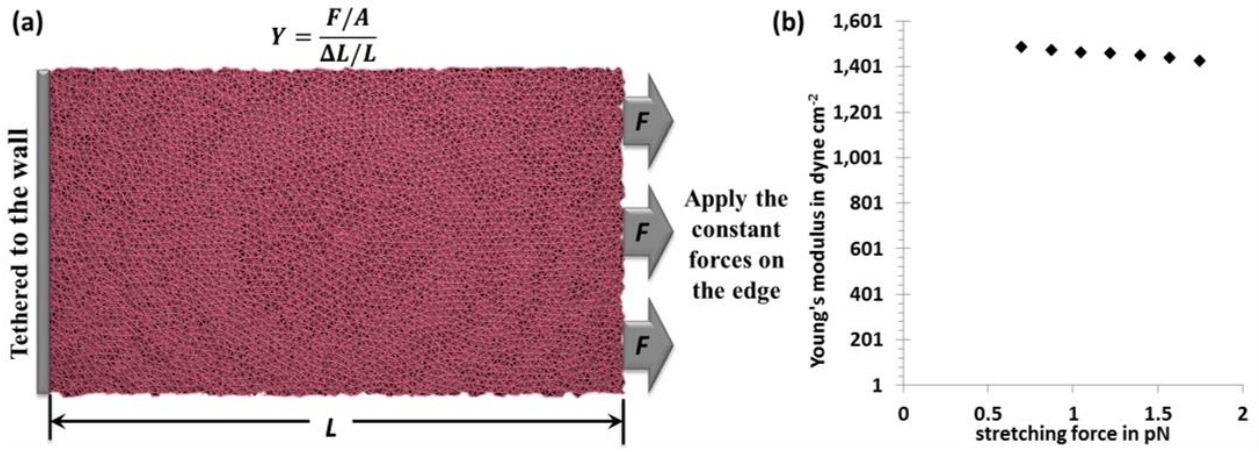

Figure 4.3: Area-stretching experiment and the elastic response of the membrane. (a) one edge of the membrane is tethered to a fixed wall and the other edge is pulled by a constant force. The Young's modulus is estimated by $Y = (F/A)/(\Delta L/L)$ in which F is the force exerted on the membrane, A is the cross-section area through which the force is applied, ΔL is the amount by which the length of the membrane changes and L is the original length. (b) Using different stretching forces for assessing the Young's modulus of the deformable membrane model with $k_{mm} = 0.00005$ kcal $mol^{-1}A^{-2}$.

The cytoplasm particles interact with only non-bonded interactions. The non-bonded LJ potential is given by $4\epsilon\left[\left(\frac{\sigma}{r}\right)^{12} - \left(\frac{\sigma}{r}\right)^{6}\right]$. The LJ potential parameters of the membrane ($\epsilon_{mm} = 1$ kcal $mol^{-1}, \sigma_{mm} = 400.0$ A) and cytoplasm ($\epsilon_{cy} = 1$kcal $mol^{-1}, \sigma_{cy} = 400.0$ A) are again chosen to be similar in order to keep the non-bonded interactions as uniform as possible. All of these values are tested in the results. The mass of each particle is uniformly chosen so as to achieve a total mass density of 1.07 g cm^{-3} which is an averaged desired density of a platelet [105].

4.4 Simulation Methods

The dynamic simulation of the filopodia formation is achieved by incrementing two important model parameters: $r_{ts,fb}$ and $\sigma_{ts,fb}$. $r_{ts,fb}$ and $\sigma_{ts,fb}$ are used to control the length (L) and the thickness (T) of filopod (Figure 4.4), respectively.

1) At simulation timestep $ts = 0$; represents a quiescent platelet.

2) Vary $r_{ts,fb}$ and $\sigma_{ts,fb}$, such that for all $ts_i < ts_j$, $r_{ts_i,fb} \leq r_{ts_j,fb}$ and $\sigma_{ts_i,fb} \leq \sigma_{ts_j,fb}$.

3) At the end of simulation $ts = ts_{max}$; represents the filopod formation on the platelet. $r_{ts,fb}$ and $\sigma_{ts,fb}$ are varied, such that at , $\max(r_{ts,fb}) = r_{ts_{max},fb}$ and $\max(\sigma_{ts,fb}) = \sigma_{ts_{max},fb}$ are attained at $ts = ts_{max}$.

By gradually increasing $r_{ts,fb}$ and $\sigma_{ts,fb}$ one can dynamically simulate longer and thicker filopod. These model parameters cannot be indefinitely extended, which may otherwise result in membrane tearing and leaking of the cytoplasm particles, thus disrupting the structural integrity of the platelet model. This specific limitation of the model can be rectified by reducing the degree of model coarsening by using a larger number of particles. The rest of the parameters remain constant during the simulation to preserve the structural integrity of the platelet during the formation of filopodia.

The simulations are performed using NAMD code designed for HPC simulations of large biomolecular systems [45]. The simulations for this particle-based system are conducted using the NVT ensemble at a steady temperature of 310K. The number of particles (N) is conserved by

considering a periodic box around the platelet and the volume (V) is kept constant throughout the simulation run. The temperature (T) stabilization which is a difficult task in simulations is achieved by using Langevin Dynamics, which adjusts the integration of force fields, for temperature control [106]. Energy minimization is performed using the conjugate gradient method to stabilize the platelet model before simulating the platelet shape change. The integration timestep size used for the simulation is 200 fs.

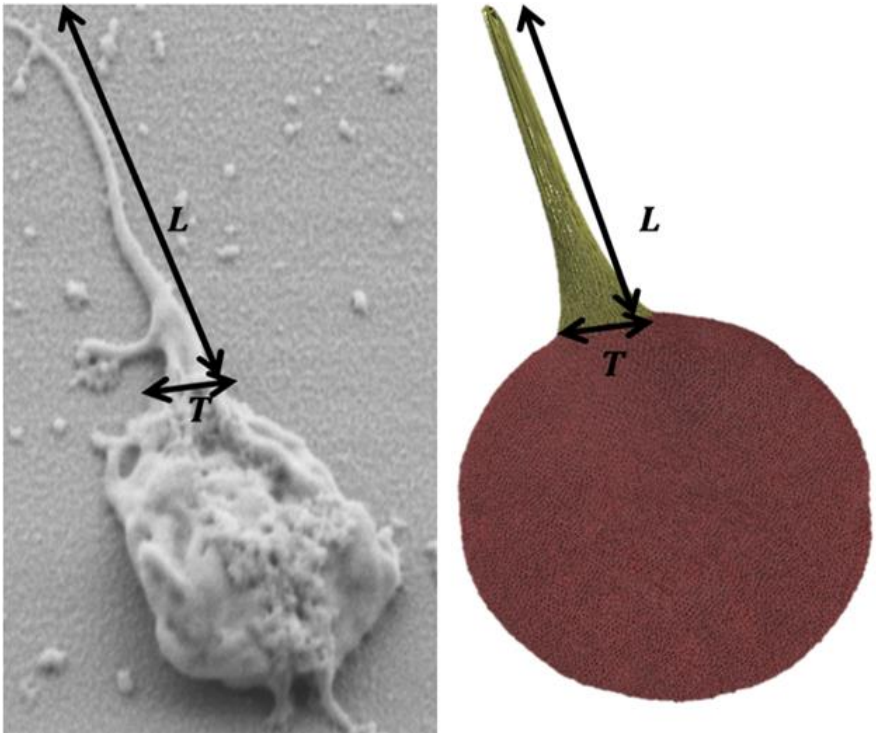

Figure 4.4: Definition of length (L) and thickness (T) of filopod in experiments and computer simulations.

The simulations are conducted to describe the impact of the model parameters ($r \triangleq r_{ts,fb}, \sigma \triangleq \sigma_{ts,fb}$) on the geometric measurements of the filopod (L, T- see *In Vitro* Experiments below), resulting in the numeric mapping correspondence between the parameters and the measurements. Accordingly, an inverse mapping scheme is constructed in which the observed

geometric measurements can be converted to the space of model parameters. After carefully studying several alternatives, the linear function f_r between r and L and quadratic function f_σ between σ and T is introduced as follows:

$$r = f_r(L) = \quad \alpha L + r_0 \qquad L \in [0, L_{max}] \qquad 4.7$$

$$\sigma = f_\sigma(T) = \begin{cases} \beta T^2 + \sigma_0 & T \in [0, T_t] \\ \sigma_{max} & T \in (T_t, T_{max}] \end{cases} \qquad 4.8$$

where α and β are two constants that can be determined for each filopod. $r_0 = 50$ A and $\sigma_0 = 90$ A. L_{max} and T_{max} are the maximum length and thickness achievable by each filopod. f_σ is continuous at $T = T_t$. Depending on the coarsening level,$\sigma_{max} = 160$ A is the maximum value for σ beyond which the filament bundles are unstable.

The change in the filopod length L is proportional to the increase in the distance between two filament bundle particles (r), thereby contributing to the linear relationship between the filopod length L and the model parameter r. Similarly, the change in the filopod cross-sectional area is proportional to the increase in the LJ potential parameter (σ) between two filament bundle particles, thereby contributing to the quadratic relationship between the filopod thickness T and the model parameter σ.

The relevant symbols and their definitions for the CGMD platelet filopod formation are summarized in Table 4.1.

Symbols	Definitions
$\mathbf{V}$	Total Energy of a particle
$\mathbf{V_B(r)}$	Total Bond Energy between two particles separated with distance r
$\mathbf{V_\theta(\theta)}$	Total Angle Energy between three particles at an angle θ
$\mathbf{U_{LJ}(r)}$	Total Non-bonded LJ potential energy
$\mathbf{k_{fc}, k_{fb}, k_{mm}}$	Spring force constant of two adjacent FC*, FB* and MM* particles respectively
$\mathbf{k_{fc\theta}, k_{fb\theta}}$	Angle force constant between three adjacent FC and FB particles respectively
$\mathbf{r_{fc}, r_{mm}}$	Distance between two adjacent FC and MM particles respectively
$\mathbf{\theta_{fc}, \theta_{fb}}$	Angle between three adjacent FC and FB particles respectively
$\boldsymbol{\epsilon_{fc}, \epsilon_{fb}, \epsilon_{mm}, \epsilon_{cy}}$	The non-bonded LJ potential parameter ϵ between two FC,FB,MM and CY* particles
$\boldsymbol{\sigma_{fc}, \sigma_{mm}, \sigma_{cy}}$	The non-bonded LJ potential parameter ϵ between two FC,MM and CY particles
$\mathbf{r_{ts,fb}}$	Variable denoting the distance between two adjacent FB particles at timestep ts
$\boldsymbol{\sigma_{ts,fb}}$	Variable denoting the non-bonded LJ potential σ between two FB particles at timestep ts
	*FC-filamentous core, FB-filament bundles, MM-membrane, CY-cytoplasm

Table 4.1: Symbols and definitions for the CGMD platelet model.

4.5 *In Vitro* Experiments

SEM images of platelets activated by exposure to flow-induced shear stresses were obtained and analyzed according to the following procedure: whole blood, 30 ml, was obtained via antecubital venipuncture from consenting healthy adult donors of both sexes as per Stony Brook University IRB-approved protocol and anticoagulated with 10% ACD-A. Gel-filtered platelets were prepared as previously described [107, 108] and diluted to a final count of 20,000/μl in HEPES-buffered modified Tyrodes solution ("platelet buffer"), with 3 mM Ca^{2+} added 10 min prior to the experiments.

The platelets were exposed to constant shear stresses of 1 dyne cm^{-2} or 70 dyne cm^{-2} for 4 min in the Hemodynamic Shearing Device (HSD), a programmable cone-plate-Couette dynamic

viscometer that generates uniform shear stress conditions [109]. Platelet samples were withdrawn after 1 min and 4 min, and immediately fixed with 1% paraformaldehyde in platelet buffer. In addition, the buffer in which the platelets were suspended contains 0.1% bovine serum albumin to block adhesion to exposed surfaces. Platelet counts were conducted before and after all experiments to ensure no platelet loss due to adhesion or lysis. Samples were placed on standard microscope slides pre-coated with poly-L-lysine (Sigma Aldrich, St. Louis, MO) for 2 hours at room temperature. Slides were gently washed twice with double-distilled H_2O and subjected to an ethanol dehydration series (0%, 25%, 50%, 75%, and 100% EtOH, with 5 min per step). The slides were then sputter-coated with islanded gold particles (6 nm thick film) in an argon-filled vacuum chamber and imaged in an SEM microscope (LEO 1550) at a 30° angle and 30,000X magnification. The resulting images were analyzed using the MATLAB image processing toolbox. Geometrical measurements of major and minor axis lengths by curve fitting of an ellipse on the platelet boundaries. Filopod boundary coordinates were manually recorded. The distance between the coordinates of this boundary which intersected those of the platelet boundary define the filopod thickness, while a morphological erosion of the area defines the filopod central axis, and ultimately its length.

4.6 Simulation Results

Section 4.6.1 shows the simulation results of a long filopod and another example where three filament bundles are used to simulate a short filopod. Corresponding model parameters are also shown for the two cases in Section 4.6.2 that discusses the model parameterization and derives

an inverse mapping scheme between the observables and model parameters for the given platelet model. Section 4.6.3 compares the simulation results with experimental results obtained through SEM image analysis of activated platelets. Section 4.6.4 discusses the performance of the CGMD platelet and filopodia formation on the supercomputers for the three test cases: long, medium and short filopodia.

4.6.1 Filopodia Formation

The platelet to enable the dynamics of filopodia formation has been modeled. This behavior is quantified by measuring the geometric features such as the length (L) and thickness (T) (Figure 4.4) of the simulated filopodia. During the activation process, the actin filaments rearrange and grow radially outward pushing the membrane to form the filopod. This phenomenon is achieved in the model by dynamically increasing the model parameter $r_{ts,fb}$ between the filament bundle particles, such that the protruding filament bundle that rests on the rigid filamentous core extends radially outward and deforms the membrane (Figure 4.5a, top row).

Simultaneously, the elastic model membrane moves to effectively encompass the protruding filament bundle. By tuning the LJ potential parameter $\epsilon_{fb} = 1000$ kcal mol^{-1}, strong repulsion localized near the membrane and filament bundle connections is achieved, preventing the tearing of the membrane. The resultant membrane evolution at various timestep (ts) is depicted (Figure 4.5a, bottom row). The top row in Figure 4.5a shows the filamentous core, filament bundle and cytoplasm inside the platelet model at the various timestep (ts).

As observed, the strong bonded forces between any two adjacent particles of the filamentous core preserved the rigid shape. Furthermore, the high angle force constant between filamentous core particles $k_{fc\theta}$ ensured strong resistance to bending. Hence, during simulation of filopod formation the protruding filament bundle that rests on the filamentous core grew radially outward and did not push down on it. The repulsive LJ potential between the cytoplasm and membrane guaranteed that no cytoplasm particles can escape outside the membrane. Also, the LJ potential between cytoplasm particles ensured the gel-like behavior of the cytoplasm inside the platelet model is preserved. By dynamically changing $r_{ts,fb}$ over the course of the simulation (Figure 4.5b, first plot), the length (L) of the filopod can be easily controlled (Figure 4.5b, third plot).

Additionally, by dynamically changing the LJ potential parameter between two adjacent particles of the protruding filament bundle $\sigma_{ts,fb}$ (Figure 4.5b, second plot) the thickness (T) of the filopod was controlled (Figure 4.5b, fourth plot). The sequence in Figure 4.5a (i)-(iv) demonstrates the effects on the shape of the platelet during filopod formation which was achieved by incrementing the model parameters $r_{ts,fb}$ and $\sigma_{ts,fb}$, illustrating the time-dependent effects of altering these parameters.

With the discretized filamentous core, a total of 59 filament bundles are constructed. By choosing one or more out of the 59 possible filament bundles, a physiological-like multiple filopodia formation can be realized. The versatility of the model is demonstrated by simulating filopodia formation of varying lengths and thicknesses, as depicted in Figure 4.6a. By equally varying the model parameters $r_{ts,fb}$ and $\sigma_{ts,fb}$ in three adjacent filament bundles, a filopod of different geometric features, L and T was realized. As observed, the filopod formed in Figure 4.6

is shorter in comparison with the filopod formed in Figure 4.5b. This was achieved by reducing the value of the model parameter $r_{ts,fb}$ (Figure 4.6c, first plot) and the composition of particles representing the three filament bundles, resulting in an overall shorter filopod (Figure 4.6c, third plot). Similarly, by equally changing the model parameter $\sigma_{ts,fb}$ (Figure 4.6c, second plot) for these three filament bundles, a wider filopod (Figure 4.6c, fourth plot) was produced. Collectively, the two representative cases in Figure 4.5 and Figure 4.6 show the variation and flexibility in simulating filopod characteristics - obtained by changing the model parameters $r_{ts,fb}$ and $\sigma_{ts,fb}$.

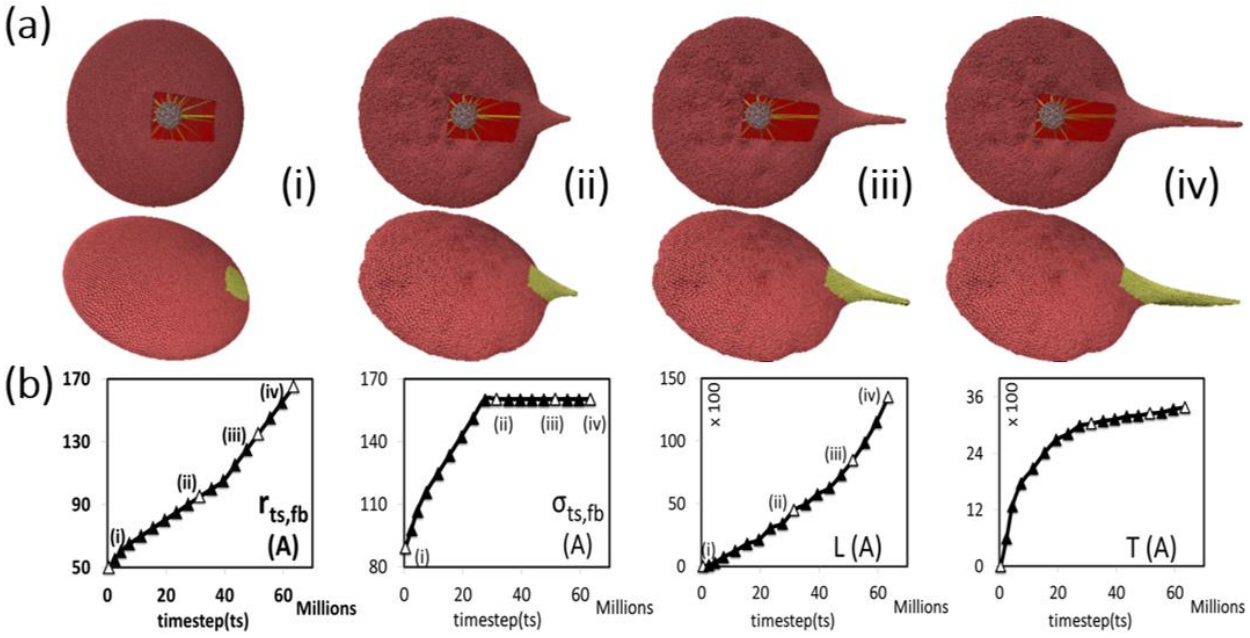

Figure 4.5: Evolving filopod formation of the platelet model. (a) The first row shows the filamentous core (white), filament bundles (yellow) and cytoplasm (red) components inside the platelet; second row is the complete platelet membrane. (b) Plot for model parameters $r_{ts,fb}$, $\sigma_{ts,fb}$ and output measurements of filopod L, T with respect to timestep ts in the simulation. The Y-axis units are Angstroms, X-axis units are number of simulation steps.

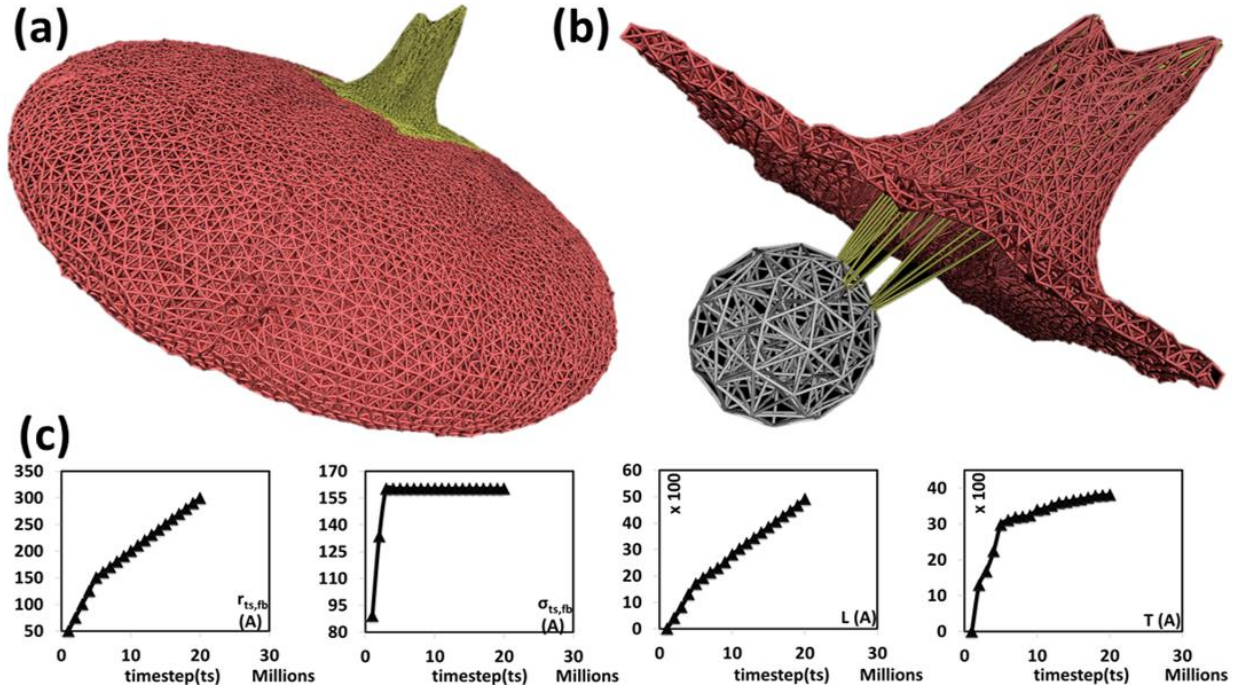

Figure 4.6: Filopod formation using three filament bundles in close proximity. (a) Complete platelet membrane after filopod formation with (b) filamentous core (white) and filament bundles (yellow) components inside the platelet. (c) Plot for model parameters $r_{ts,fb}, \sigma_{ts,fb}$ and output measurements of filopod L, T with respect to timestep ts in the simulation. The vertical axis units are Angstroms; horizontal axis units are number of simulation steps.

4.6.2 Model Parameterization

The inverse mapping scheme defined in Section 4.4 hypothesizes a linear relationship between the model parameter r and the filopod length L and a quadratic relationship between the model parameter σ and the filopod thickness T. Intuitively, the length of the filopod (L) is controlled by the distance between a pair of particles on the straight filament bundle (r) and hence a linear relationship is postulated. The cross-sectional area of filopod (proportional to T^2) is

controlled by the LJ potential parameter (σ) between two filament bundle particles. The coefficient of determination (R^2) is proposed to measure the relationships between the thickness and model parameter.

Figure 4.7 shows the instantaneous lengths and thicknesses (shown in black) of the two representative cases describing the formation of a long filopod (Figure 4.5) and a short filopod (Figure 4.6), respectively. The plot of the linear function f_r (Equation. 4.7) between the geometric measurement L and the model parameter r is derived ($R^2 > 96\%$). Similarly, the plot of the quadratic function f_σ (Equation. 4.8) between the geometric measurement T and the model parameter σ is derived ($R^2 > 98\%$). Similarly, the plot of the quadratic function f_σ (Equation. 4.8) between the geometric measurement T and the model parameter σ is derived ($R^2 > 98\%$). The constants α and β are dependent on the coarse-graining level of filament bundles used to simulate the filopod formation. Thus, the constant α for both of the filopodia is determined by fitting a linear function f_r as shown in Figure 4.7a. Similarly, the constant β for both of the filopodia is determined by fitting a quadratic function f_σ as shown in Figure 4.7b. In this framework, depending on the model structure and the coarsening level, the constants $\alpha \in [0.95 * 10^{-2}, 5.26 * 10^{-2}]$ and $\beta \in [0.8 * 10^{-5}, 3.0 * 10^{-5}]$. This represents the physiologically possible range of filopodia formation patterns that can be simulated by this model, within the current limits of the membrane stability and structural integrity of the model.

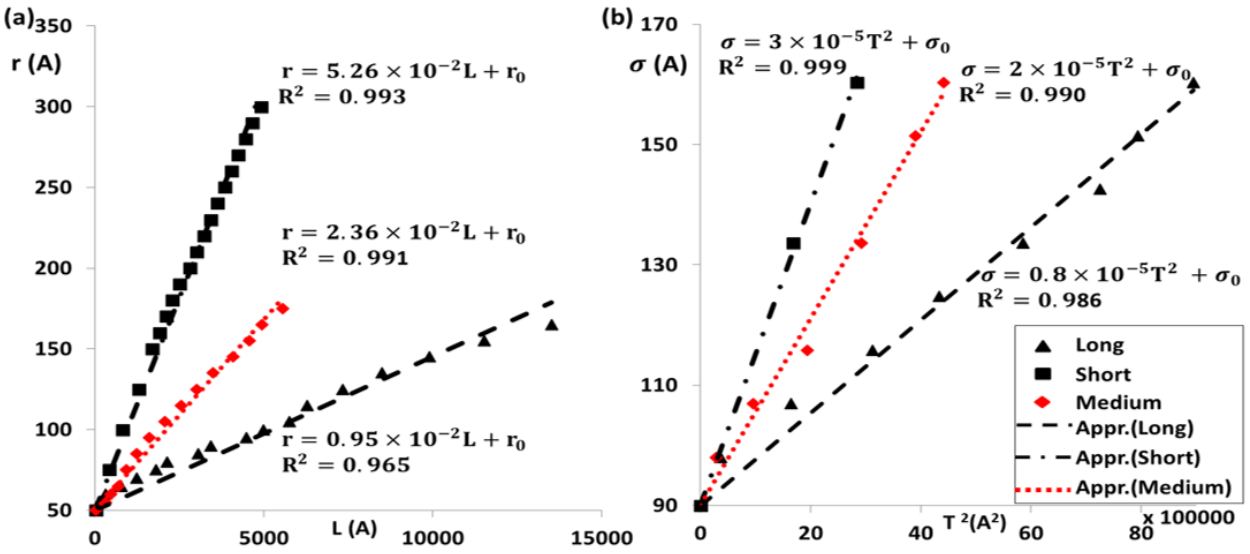

Figure 4.7: Correlation between model parameter space and experimental measurements. Plots for the (a) linear function f_r between the model parameter r and the observed geometric measurement L of the filopod. (b) Quadratic function f_σ between the model parameter σ and the observed geometric measurement T^2 of the filopod for the two representative cases in Figure 4.5 and Figure 4.6 (shown in black). Also the results for the filopod of medium length (shown in red) are plotted. The units of r, σ, L, T are in Angstroms.

In Figure 4.8, simulation snapshots of a medium sized filopod are shown. The linear function $f_r$and f_σ for this filopod are plotted in Figure 4.7a and Figure 4.7b (shown in red). The corresponding α and β values fall in the range shown above.

Figure 4.8: Platelet membrane after filopod formation using an intermediate filament bundle.

An extensive experimental database of platelet activation consisting of geometrical measurements of filopodia for different shear stress-exposure time combinations will expand this parameter space. With such data, one can use the framework established above that gives independent inverse mapping functions f_r and f_σ. Given a desired experimental measurement L for a filopod, the linear function f_r will generate corresponding model parameter r. The maximum length of the filopod that can be simulated by the model is limited by the coarsening level and elasticity of the model membrane. Similarly, given a desired experimental measurement T, the quadratic function f_σ will generate corresponding model parameter σ. With such a framework, one can simulate the dynamic growth of filopodia of desired lengths and thicknesses observed in platelets that are exposed to varying levels of shear stress-exposure time combinations.

4.6.3 Model Verification

In Figure 4.9, three examples of the dynamic simulation results achieved by the end of the simulation time (corresponding to the experimental exposure time of the platelets to a prescribed level of shear stress), are compared to the geometric features of the measurements of filopodia formation (length and thickness) processed from SEM images of the exposed platelets. These images were obtained from the flow-induced shear stress experiments conducted using the HSD. While the simulations depict the dynamic formation of the filopodia, the comparisons are of snapshots from the dynamic simulations corresponding to the experimental endpoints.

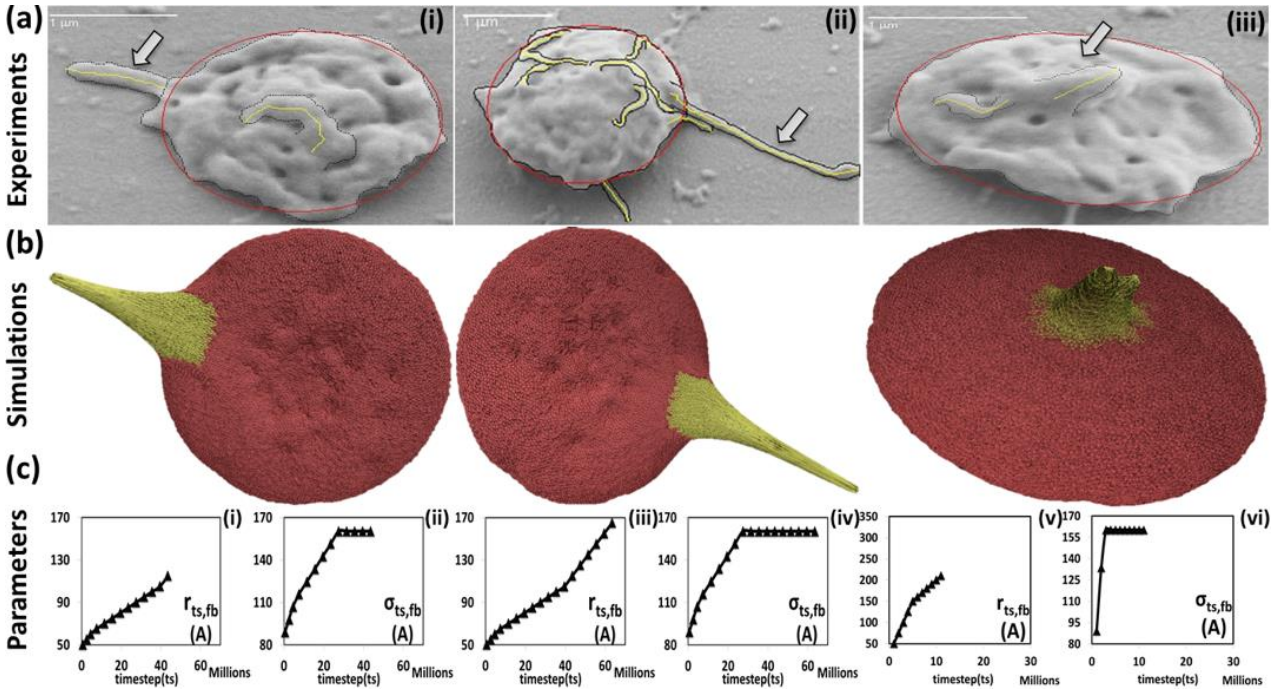

Figure 4.9: Visual comparisons of experimental and simulated filopod formation. (a) SEM images at (i) 1 dyne cm^{-2} - 4 min (ii) 70 dyne cm^{-2} - 4 min (iii) 70 dyne cm^{-2} - 1 min. Tracings of the images in panel (a) illustrate the retained ellipsoidal shape of the platelet and filopod formation. The length (L) and thickness (T) are observed to be (i) 0.68 and 0.29 μm (ii) 1.39 and 0.35 μm and (iii) 0.29 and 0.32 μm, respectively. (b) Simulated filopod formation on model platelet. (c-i to c-vi) The graphs represent the model parameters for the three simulations. The Y-axis units are Angstroms; X-axis units are number of simulation steps.

As shown in Supporting Data S1, when the platelets undergo shear stress (1 dyne cm^{-2} and 70 dyne cm^{-2}) for exposure times (1 min and 4 min), they maintain the discoid shape and have filopodia extending from the membrane. Following the shear experiments the platelets were immediately fixed in 1% paraformaldehyde for at least 30 minutes prior to placing on poly-L-lysine coated slides for SEM studies, and it is not expected that the focal adhesions triggered any additional platelet shape change. Under the given pathological shear stress levels for extended periods of time, the filopodia length range from 0.24-2.74μm and thickness range from 0.06-

0.73μm were observed. The SEM images of platelets exposed to (i) 1 dyne cm^{-2} - 4 min (ii) 70 dyne cm^{-2} - 4 min (iii) 70 dyne cm^{-2} - 1 min are shown in Figure 4.9a. The snapshots of the platelet model during the simulation of the filopodia formation are shown in Figure 4.9b. The images were compared visually with the SEM images from Figure 4.9a. The model is able to simulate various filopodia formations and appear to be in complete agreement with the combination of experimental conditions of shear stress levels and exposure times in which the experiments were conducted. The evolution of the corresponding model parameters $r_{ts,fb}, \sigma_{ts,fb}$ is shown up to the corresponding timestep ts_{max} in Figure 4.9c (i)-(vi). The comparison shows that while the model was not formulated to include the physiological growth mechanism of filopodia formation by actin polymerization, rather mimic the process, it successfully generated the dynamics of filopodial activity such as its initiation and extension.

4.6.4 Performance Discussion

The simulations in this chapter used a cluster of 650 nodes in which each node contains two 3.06GHz Intel Xeon 6-core CPU and 36GB of memory and networked by Infiniband QDR. the wall clock time (in seconds) for three representative simulation cases (long, medium and short filopod) are measured . The speed and speedups for varied numbers of processor cores are calculated. Speed of a simulation case using N processor cores S(N) is defined as the number of simulation timesteps per second. Speedup of the simulation on N processor cores is then given by S(1)/S(N). Figure 4.10a and Figure 4.10b show the speeds and speedups of the three simulations for different numbers of processor cores. The performance results showed that the maximum speedup can be up to 52 for the present problem size and then the speedup curve greatly reduces

along with the increase of processors cores. This drop indicates that the communication system becomes a dominant cost when more nodes are used.

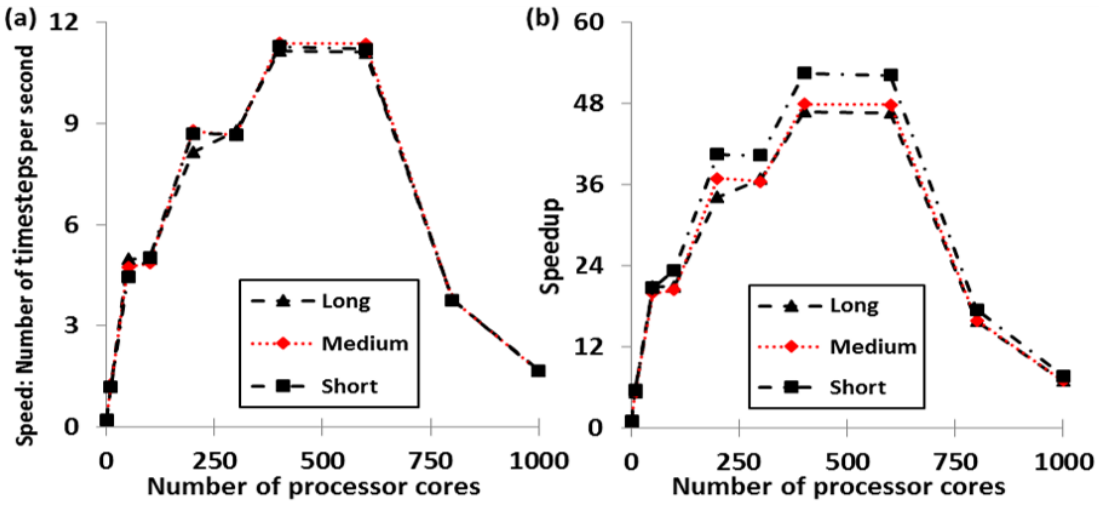

Figure 4.10: The scalability of the simulation of three representative filopodia simulations (long, medium and short filopodia) measured by (a) Speed vs. Number of cores and (b) Speedup vs. Number of Cores.

Chapter 5

Quantitative Model of Platelet Shape Change

5.1 Platelet Shape Change during Activation

Cardiovascular diseases cause approximately 32% of deaths in the US annually [110]. Implantable blood recirculating devices provide a lifesaving solution for these diseases. However, such devices require life-long anticoagulation treatment due to the related thrombotic complications [28, 111]. The mechanism for thromboembolic complications is similar to that of the vascular disease processes, where, thrombosis occurs due to interaction of blood components with injured vascular wall and the non-physiological flow patterns in cardiovascular pathologies. The ensuing initiation and enhancement of the hemostatic response is caused by chronically activated platelets. Similarly, pathological flow patterns [112, 113] and contact with foreign surfaces cause thromboemboli in these devices. The former appears to be a more prominent contributor towards platelet activation.

Due to the pathological flow patterns generated in these devices [22], platelets experience varied shear stresses causing activation and aggregation. The manufacturers of these devices test and optimize for hemolysis, a phenomenon occurring at shear stress levels much higher (ten-fold) than those for platelet activation [114, 115]. These blood-recirculating devices need to be optimized for lower-level shear flow-induced thrombogenecity [116, 117]. In order to understand

and quantify the effect of shear-induced flow, various studies have formulated platelet activation functions based on experimental observations. The first attempt to study blood damage and hemolysis as a function of shear stress and exposure time was proposed using the well-known power law [118], a first-order approximation. This work influenced many later studies on the effects of shear stress-exposure time on RBCs and platelet activation [27, 119-121]. Platelet activation was also measured by stress accumulation (SA) models that are defined as a product of shear stress and exposure time [122]. SA models have been used in experimental validation [118] and numerical simulations [26, 123, 124]. Recently, Platelet activation state (PAS), a measure of thrombin generation utilizing chemically modified prothrombin [125], was used for studying the platelet activity in devices [107, 126], flow loops and stenosis [127] under various shear stress-exposure time combinations.

At the cellular level, a bottom-scale model to better understand the role of platelets in thrombosis can be developed by examining the dynamic shape change due to the filopodial growth from the platelet surface. The filopodia grow as a reaction to the extracellular environment that potentiates the interaction with other nearby platelets in its surroundings. A major step in elucidating the rules of platelet activation is to understand the filopodial growth on platelets in response to these external cues. Substantial information regarding the shear flow-induced platelet activation can be obtained by observing the filopodia generation in their *in vivo* milieu. However, the filopodial growth and the shape change of platelets cannot be recorded by continuously tracking them in such flows. Thus, it is difficult to discern the fundamental mechanisms of filopodial growth by observing them during their development. Hence, considerable information regarding platelet shape change can be obtained only by analyzing the filopodial growth in a

simplified *in vitro* environment, and then establishing mathematical models for the "end-point" results to predict behavior in more complex *in vivo* conditions. The experimental observations given by platelet morphometrics are analyzed to establish a quantitative model for lower-level shear-induced platelet activation.

5.2 A Platelet Morphometric Model

The joint effects of both the shear stress and the exposure time on platelet morphological change are poorly understood. Coupling with laboratory experimental insights in observing the platelet morphometry during shear flow-induced activation, the platelet changes to formulate a morphometric model are quantified. Observations of *in vitro* platelet shape change through SEM images reveals two distinguishable regions of morphology: (a) a thin circular body of diameter 2-3 μm that is referred to as "central body" and (b) a thin finger–like micro projections of up to 2 μm in length that are called "filopodia".

5.2.1 The Filopodia Growth Model

The quantitative model developed here is an attempt to determine the growth of filopodia, measured in longitudinal direction, in response to the independent shear stress and exposure time conditions. By introducing a simple analytical growth function, the link between the actin monomer polymerization [13, 128] with the formation of filopodia necessary to drive platelet morphological changes is shown. Inspired by the conventional laboratory experiments and guided

by several essential basic principles in mathematics and biophysics, an analytical formula for expressing the growth of platelet filopodia is derived.

Conversely, like most model builders, the results obtained are corroborated by employing the model with the expected measurements of growth under practical and idealized laboratory conditions. Platelets are usually not activated in the blood circulation of a healthy person, but when the blood is drawn, shear stress will be self-imposed and activation will likely occur. To accommodate this unavoidable process, this model builds in an additional (initial) filopod length (L_0) in incorporating gratuitously at the start of imaging and this additional length stays constant during the course of experiment. Thus, the observed filopod length $L(\tau, t)$ during the actual experiments is the sum of the theoretical filopod length $\mathbb{L}(\tau, t)$ with the initial length L_0:

$$L(\tau, t) = \mathbb{L}(\tau, t) + L_0 \tag{5.1}$$

This model building is based on the following observations. As in logistic equation, for a given stress level, the expected growth rate of filopod is defined by the following initial value problem:

$$\begin{cases} \dfrac{d\mathbb{L}(t)}{dt} = \alpha\big(\mathbb{L}(t)\big)\left(1 - \dfrac{\mathbb{L}(t)}{L_m}\right) \\ \mathbb{L}(t = 0) = \mathbb{L}_0 \end{cases} \tag{5.2}$$

where $\mathbb{L}(t)$ is the filopod length at the exposure time (t), α characterizes the growth rate and L_m is a (constant) length limit. Physiologically, this growth can be attributed to the rapid assembly of actin monomers near the plasma membrane to stack up to form the filopod during the initial stages of activation [129] as indicated by the linear term ($+\alpha\mathbb{L}(t)$). However, by conservation of total number of free actin monomers in a given platelet [13, 129], the filopodia growth diminishes as it

progresses, as expressed by the quadratic term ($-\frac{\alpha \mathbb{L}^2(t)}{L_m}$). Since it is difficult to determine the number of actin monomers inside the platelet at any given time of growth, another way of introducing the limiting factor into the growth equation can be the length limit (L_m) given the external stimuli (shear stress-exposure time conditions) and stability of the platelet. The growth rate α is the intrinsic growth parameter of the platelet and dependent on the polymerization of actin monomers to form filopodia. The parameter L_m is the maximum sustainable increase of the filopod length and it depends on the flow-induced shear stress (τ) and other external and internal conditions.

The initial value problem (2) is one of the broad applications of the logistic equation such as the Verhulst-Pearl equation [130] that defines the growth rate of this self-limiting biological system as proportional to the current length of the filopod $\mathbb{L}$ and also the diminishing capacity of the platelet to extend the filopod beyond the length limit L_m. Previous works have used the actin polymerization and depolymerization rates to quantify the rates of filopodia growth on cells without considering any special chemical or mechanical stimuli [88, 90].

The parameters ($\mathbb{L}$, L_m) can be obtained by such lower-order MD based principles but, given the dynamic nature of the external stimuli in this problem, and the lack of data on how they influence the actin behavior, a large approximation has to be made to make it practical. Instead, the model resulrs are matched with laboratory experiments following the well-practiced fourth paradigm [131] for scientific discovery through observable data.

The initial value problem (2) can be solved easily,

$$\int_{\mathbb{L}_0}^{\mathbb{L}} \frac{L_m d\mathbb{L}(t)}{\mathbb{L}(L_m - \mathbb{L})} = \alpha \int_0^t dt \tag{5.3}$$

$$\int_{\mathbb{L}_0}^{\mathbb{L}} \left(\frac{1}{L_m - \mathbb{L}} + \frac{1}{\mathbb{L}}\right) d\mathbb{L} = \alpha t \tag{5.4}$$

Solving for $\mathbb{L}$, we get

$$\mathbb{L}(t) = \frac{L_m}{1 + \left(\frac{L_m}{\mathbb{L}_0} - 1\right) e^{-\alpha t}} \tag{5.5}$$

Introducing a new shear stress-dependent parameter t_c that measures a critical time at which the growth rate of filopod peaks:

$$\frac{L_m}{\mathbb{L}_0} - 1 = e^{\alpha t_c} \tag{5.6}$$

we get

$$\mathbb{L}(t) = \frac{L_m}{1 + e^{-\alpha(t - t_c)}} \tag{5.7}$$

Thus for a given shear stress level (τ) and exposure time (t) the observed filopod length $L(\tau, t)$ is given by:

$$L(\tau, t) = L_0 + \frac{L_m(\tau)}{1 + e^{-\alpha(t - t_c(\tau))}} \tag{5.8}$$

This seemingly simple filopod length function embodies a rich set of relationships among the exposure time, shear stress, and the length. The length limit $L_m(\tau)$, expectedly, is proportional to the external shear stress τ applied to trigger the platelet morphological change. This can be

attributed the increased mechanical stimulus experienced by the platelet thereby resulting in more actin monomer polymerization and increased filopod length limit. On the other hand, for the critical time t_c, a higher shear stress, requires a shorter time to achieve maximal growth rate and thus the critical time should be a function of τ.

Figure 5.1 describes the effects of τ-dependent variables L_m and t_c on the filopod length $L(\tau, t)$ (Figure 5.1a) and filopod growth rate $\frac{d}{dt}L(\tau, t)$ (Figure 5.1b) when all other variables in Equation. 5.8 are held constant. Figure 5.2 shows the filopod length $L_\tau(t)$ and the growth rate $\frac{d}{dt}L_\tau(t)$ as a function of time for a given shear stress (τ). At $t = t_c$ growth rate peaks and the filopod length $L_\tau(t) = L_0 + \frac{L_m}{2}$.

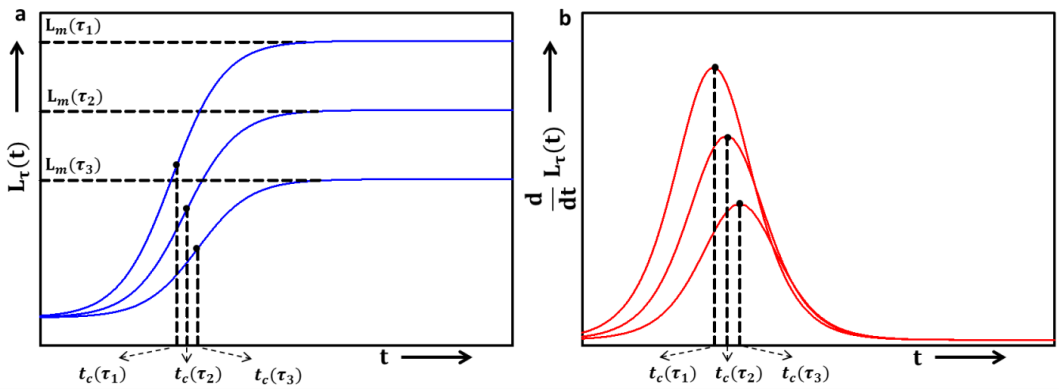

Figure 5.1: Effects of length limit and critical time on filopod length and growth rate. **(a)** the filopod Length $L_\tau(t)$ (shown in blue) and **(b)** the growth rate $\frac{d}{dt}L_\tau(t)$ (shown in red) as a function of exposure time, where $(\tau_1 > \tau_2 > \tau_3)$.

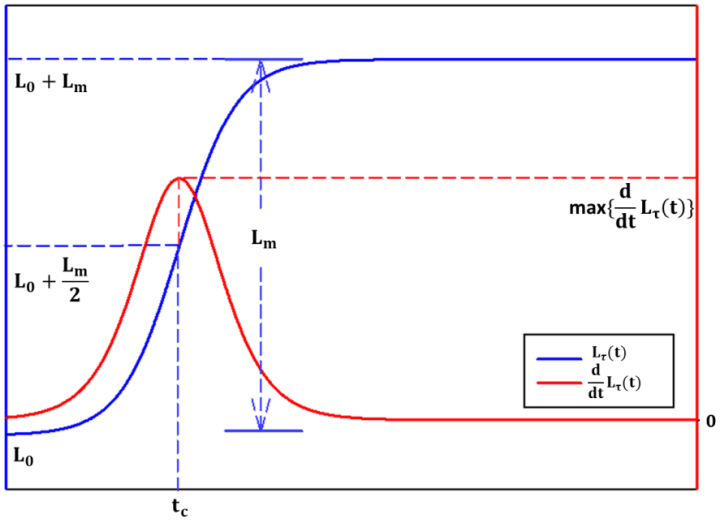

Figure 5.2: Filopod Length and growth rate as a function of shear stress and exposure time. $L_\tau(t)$ (Shown in blue) and the growth rate $\frac{d}{dt} L_\tau(t)$ (shown in red).

The relevant symbols and their definitions for the Filopodia Growth Model are summarized in Table 5.1.

Symbols	Definitions
$\boldsymbol{\tau}$	Shear stress
$\mathbf{t}$	Exposure time
$\mathbf{L}(\boldsymbol{\tau}, \mathbf{t})$	observed filopod length at shear stress (τ) and exposure time (t)
$\mathbb{L}(\boldsymbol{\tau}, \mathbf{t})$	experimental filopod length at shear stress (τ) and exposure time (t)
$\mathbf{L_0}$	initial filopod length
$\mathbf{L_m}(\boldsymbol{\tau})$	filopod length limit at shear stress (τ)
$\mathbf{t_c}(\boldsymbol{\tau})$	critical time at which the growth rate of filopod peaks at a shear stress (τ)

Table 5.1: Relevant symbols and definitions for the Filopodia growth model

5.3 Experimental Validation

In section 5.3.1, the details of the laboratory experiments and the imaging techniques used are presented. In section 5.3.2, the parameters of the morphometric model proposed in Section 5.1 from the experimental results are determined. In section 5.3.3, important morphology measurements, circularity and filopodia number is presented. In Section 5.3.4, the correlation between the chemical activity measurement given by PAS and the morphological change is discussed.

5.3.1 *In Vitro* Experiments

Whole blood, 30 ml, was obtained via antecubital venipuncture from consenting healthy adult donors of both genders as per a Stony Brook University IRB-approved protocol and anticoagulated with 10% ACD-A. Gel-filtered platelets were prepared as previously described [132, 133] and diluted to a final count of 20,000/μl in HEPES-buffered modified Tyrodes solution ("platelet buffer"), with 3 mM Ca^{2+} added 10 min prior to experiments. The platelets were exposed to constant shear stresses of 10, 20, 30, 40 and 50 dyne cm^{-2} for 4 min in the HSD, a programmable, dynamic cone-plate-Couette viscometer that generates uniform shear stress conditions [134, 135]. Platelet samples were withdrawn at start and after 0, 15, 30, 45, 60, 120, 180 and 240 s, and immediately fixed with 2% glutaraldehyde in platelet buffer or prepared for platelet activity measurements. In addition, the buffer in which the platelets were suspended contains 0.1% bovine serum albumin to block adhesion to exposed surfaces. The platelet counts were counted before and after all experiments to ensure no platelet loss due to adhesion or lysis.

Platelet morphological measurements

Fixed samples were placed on standard microscope slides pre-coated with poly-L-lysine (Sigma Aldrich, St. Louis, MO) for 2 hours at room temperature. Slides were gently washed twice with double-distilled H_2O and subjected to an ethanol dehydration series (0%, 25%, 50%, 75%, and 100% EtOH, with 5 min per step). The slides were then sputter-coated with islanded gold particles (6 nm thick film) in an argon-filled vacuum chamber and imaged in an SEM microscope (LEO 1550) at a 30° angle and 30,000× magnification. The SEM images were analyzed using the NIH ImageJ software [136]. Geometrical measurements of the major and minor axis lengths of the central body are evaluated by curve-fitting of an ellipse on its boundary. Filopod lengths were evaluated from the tip to the base at the boundary of the central body using the segmented line tool on ImageJ. True lengths were calculated by setting pixel ratio as defined by the scale on the SEM images. Also the number of filopodia per platelet is recorded. Figure 5.3 shows, as an example, the image analysis of a platelet exposed 20 dyne cm^{-2} and 120s.

Platelet activity measurements

PAS of shear-exposed platelets was assayed using a modified prothrombinase-based colorimetric method which quantifies the absorbance of a defective form of thrombin that does not further activate platelets, but is instead used as a marker [107]. PAS for each time point was normalized against the PAS value of fully-activated platelets, obtained by sonication of an unsheared platelet sample at 10 W for 10 s (Branson Sonifier 150 with microprobe, Branson, MO, USA) [108, 134]. Normalized PAS is therefore represented as a fraction, with a maximum value of 1.0. Results are presented in Section 5.3.4.

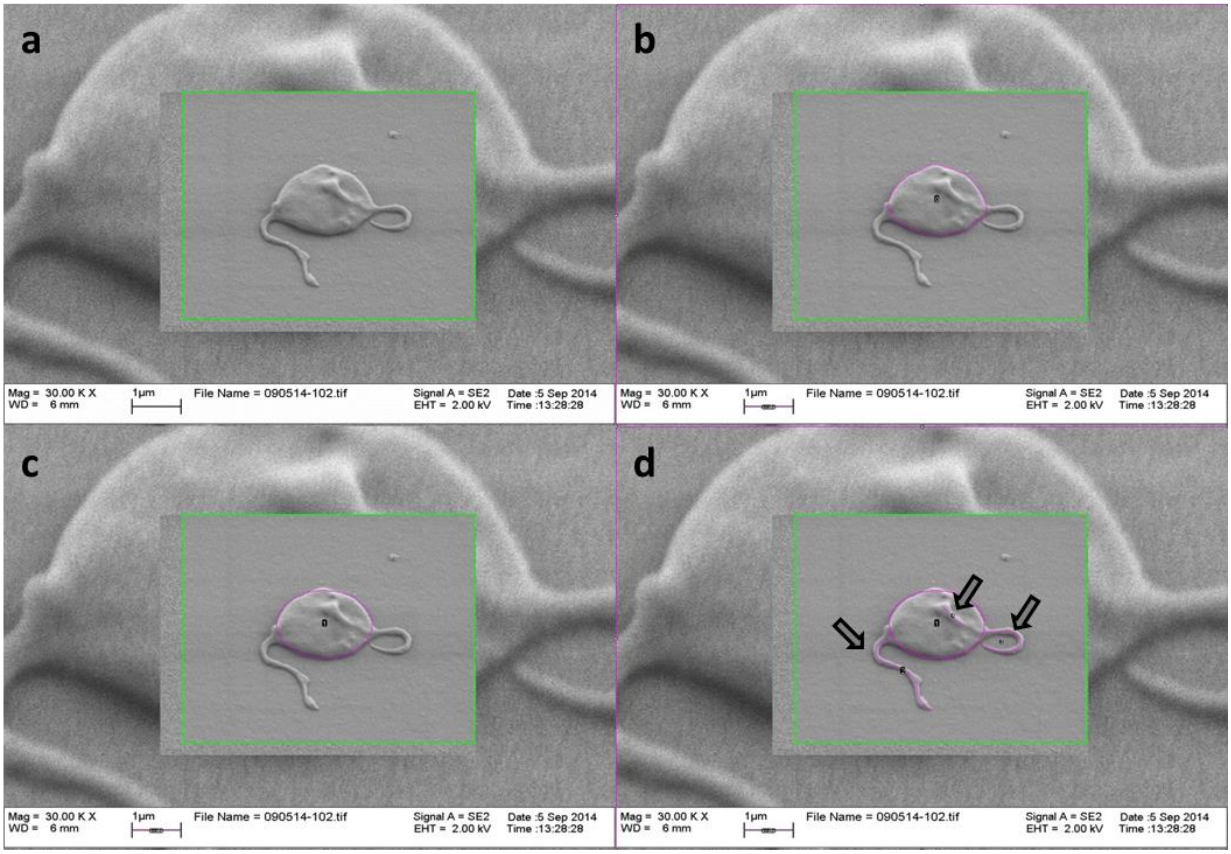

Figure 5.3: SEM image analysis using ImageJ toolbox. (a) SEM image of a platelet exposed to 20 dyne cm^{-2} for 120 s. (b) Platelet central body boundary marked. (c) Fitting the ellipse for the central body boundary using the *Fitting Ellipse* on the ImageJ toolbox. (d) Marking the visible filopodia using the *Segmentation Tool* on the ImageJ toolbox.

5.3.2 Determination of parameters

Neither the length limit (L_m), nor the critical time (t_c) at different shear stress levels are known *a priori*. Both parameters depend on the individual platelets and their response to external stimuli triggering the platelet morphological change. They have to be determined by experimental measurements of filopod length at increments of shear stress and exposure time conditions. In the

experiments conducted, platelets were exposed to incremental shear stresses (10, 20, 30, 40 and 50 dyne cm^{-2}). Also, at each shear stress level, the platelets were exposed to incremental exposure time (0, 15, 30, 45, 60, 120, 180, and 240 s). Platelets exposed to such conditions were sampled and analyzed using the SEM techniques discussed in Section 5.3.1. Filopod lengths, major and minor axes and filopodia count were measured using ImageJ. Figure 5.4 (n=7-10) shows the mean± standard error of the means (S.E.M) of the filopod length at different shear stress levels and exposure time.

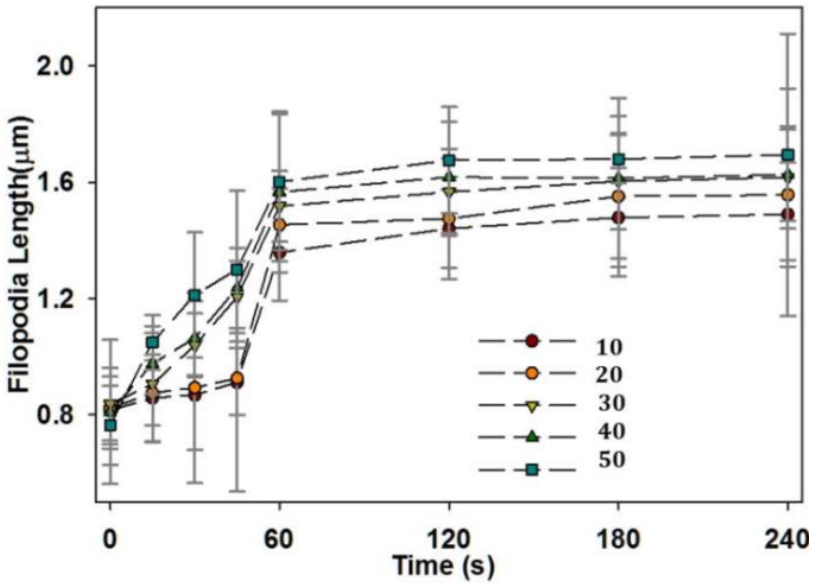

Figure 5.4: Experimental measurements of (Mean±S.E.M) of filopod length (μm) for various shear stress (10, 20, 30, 40 and 50 dyne cm^{-2}) and exposure time (0, 15, 30, 45, 60, 120, 180 and 240 s) combinations.

As in typical inverse problems, the unknown parameters that minimize the root mean square errors (RMSE) are calculated. Table 5.2 lists the unknown parameters of Equation. 5.8 for the individual stress levels along with the RMSE.

τ	L_0	L_m	α	t_c	RMSE
10	0.808	0.673	0.1	53	0.055
20	0.808	0.737	0.1	51	0.072
30	0.808	0.790	0.1	44	0.043
40	0.808	0.813	0.1	40	0.051
50	0.808	0.852	0.1	34	0.075
				Total	0.296

Table 5.2: The estimates for the unknown coefficients for the Equation 5.8 are listed for individual shear stress levels. Also, the corresponding RMSE that estimates the accuracy of the model fit is listed.

There is no discernable method by which the relationship between L_m and a given shear stress τ can be pre-determined. Intuitively, one can hypothesize that at increasing shear stress levels, there is an increase in the actin monomer polymerization in a platelet resulting in longer filopod formation. Similarly, for higher shear stress levels, a shorter time is required for actin monomer polymerization leading to faster filopod formation. Based on the experimental observations (in Table 1), the relationships of the variable parameters L_m vs. τ and t_c vs. τ are proposed as follows:

$$L_m(\tau) = \frac{1}{2}\tau^{0.1322}$$

$$t_c(\tau) = 60 - \frac{1}{2}\tau \qquad 5.9$$

The significance of such functional forms and the coefficients is not apparent; answering these questions will be a topic of future studies. Figure 5.5a and Figure 5.5b show the various

values of L_m and t_c for the experimental shear stress levels (10-50 dyne cm^{-2}), and the fits given by Equation. 5.9.

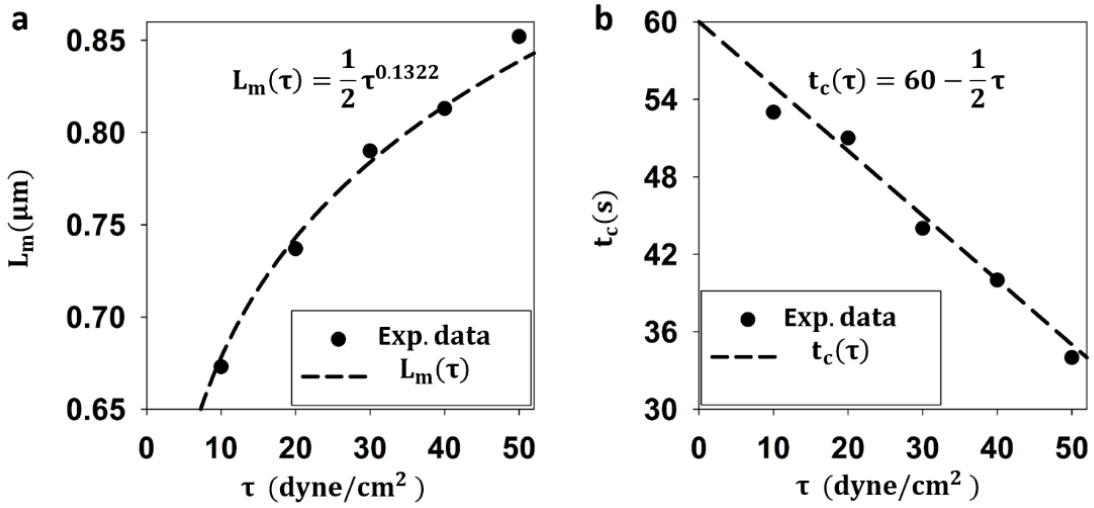

Figure 5.5: Plots of the length limit and exposure time. (a) the length limit (L_m) as a function of shear stress (τ) and the experimental values of L_m's and the (b) exposure time (t_c) at which maximal growth occurs as a function of shear stress (τ) and the experimental values of t_c's for the different shear stress levels.

The final relationship between the filopod length (μm) as a function of shear stress (dyne cm^{-2}) and exposure time (s) is given by:

$$L(\tau, t) = L_0 + \frac{L_m(\tau)}{1 + e^{-\alpha(t - t_c(\tau))}}$$

$$L_0 = 0.808$$

$$L_m(\tau) = \frac{1}{2}\tau^{0.1322} \qquad 5.10$$

$$t_c(\tau) = 60 - \frac{1}{2}\tau$$

Figure 5.6 shows the 3D plot of the $L(\tau, t)$ (μm) as a function of τ (10-50 dyne cm^{-2}) and t (0-240 s). The experimental measurements of the mean of filopod length and the residues that define the distance between the experimental measurement and model are also shown.

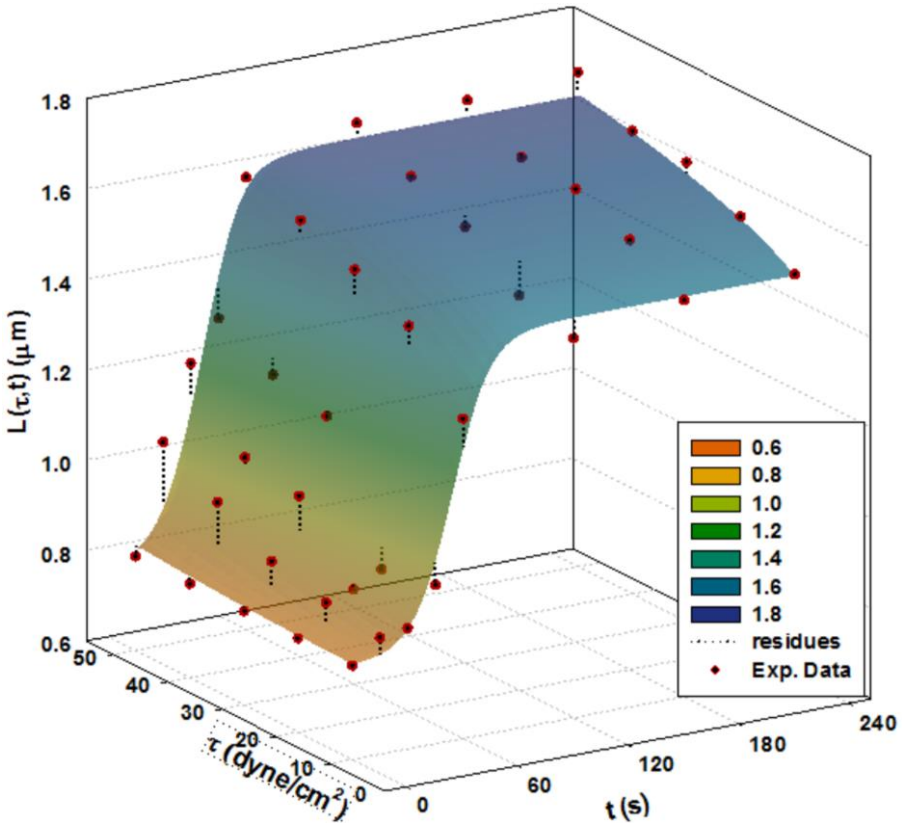

Figure 5.6: Filopod Length $L(\tau, t)$ as a function of shear stress (τ) and exposure time (t). Also shown are the experimental measurements of average filopod length (shown in red) and the residues from the modeled $L(\tau, t)$ (shown as dotted line).

5.3.3 Central Body Characteristics and Filopodia Number

For the SEM images of platelets, the central body boundary is curve-fitted by an ellipse using the *Fit Ellipse* tool in ImageJ. The platelet's central body characteristics are measured by

two metrics, circularity and major axis. Circularity is defined as $4\pi * \frac{\text{Area}}{\text{Perimeter}^2}$, where the area and perimeter are of the fitted ellipse. Circularity ranges from 0 to 1, with values closer to 0 indicating an elongated shape and values closer to 1 indicating a circular shape. Figure 5.7 (n=7-10) shows the mean ± S.E.M of circularity and major axis (of the fitted ellipse) for the shear stress levels (10-50 dyne cm^{-2}) for exposure time (0-240 s). The mean circularity ranges from (0.970, 0.992) and the mean major axis ranges from (1.992 μm, 3.083 μm) suggesting that the platelet's central body remains largely circular for the shear stress-exposure time combinations.

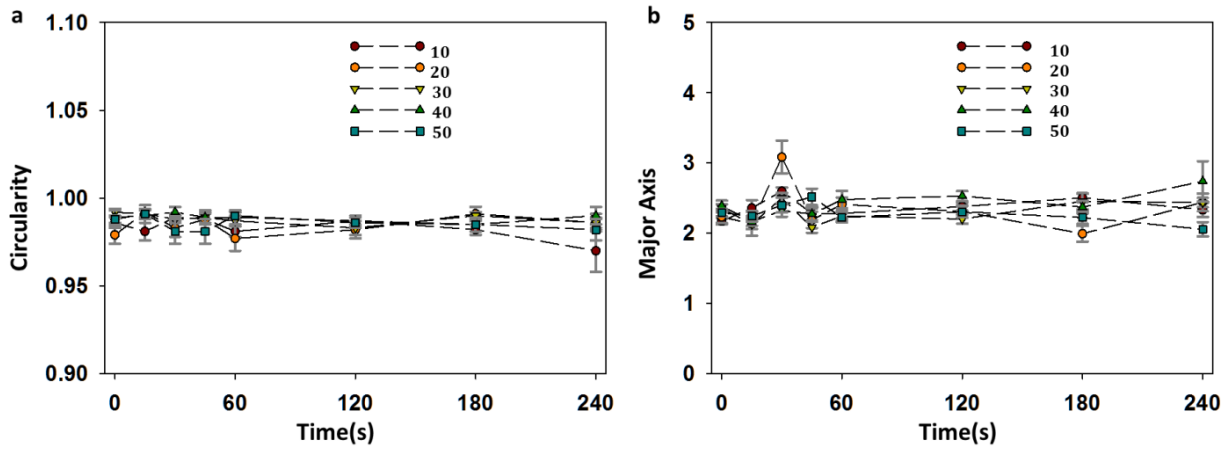

Figure 5.7: Experimental measurements of (a) circularity and (b) major axis for the various shear stress (10, 20, 30, 40 and 50 dyne cm^{-2}) and exposure time (0, 15, 30, 45, 60, 120, 180 and 240 s) combinations.

The filopodia number on a given platelet before and after exposure to the shear stress-exposure time combinations was also recorded. Figure 5.8 shows the frequency of filopodia number for the experiments conducted. The average filopodia number is between 2-3 and 90% of the filopodia number fall between 0-5.

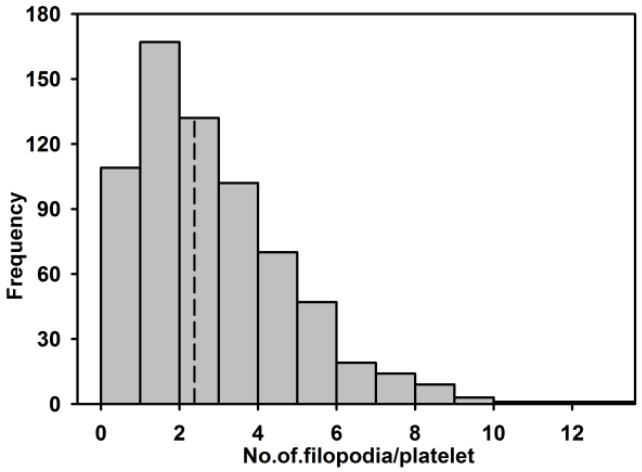

Figure 5.8: Histogram showing the number of filopodia per platelet and their frequency for the complete set of experiments. The average filopodia number is in between 2-3 filopodia.

5.3.4 Correlation between Morphological Change and PAS

The results of PAS for each shear stress condition are shown in Figure 5.9a (n = 5). The difference in PAS between samples at t=0 and t=240 s, ΔPAS, was obtained for each shear stress condition (Figure 5.9b, n = 5). These values were compared using one-way ANOVA with Tukey's *post hoc* test, where significance is established at $p < 0.05$. Significant increases in ΔPAS were observed for the 30 dyne cm^{-2} ($p < 0.05$), 40 dyne cm^{-2} ($p < 0.001$), and 50 dyne cm^{-2} ($p < 0.001$) experiments compared to 10 dyne cm^{-2} exposure. The correlations between the filopod lengths measured in Section 5.3.2 with PAS values for each time and for all shear stress exposures are done using the Pearson correlation coefficient (ρ), where its value of 1.0 represents complete correlation and 0.0 represents no correlation. For the exposure time range from 0 to 240 s, $\rho = 0.667$ (Figure 5.9c). However, by restricting these correlations to the range 0 to 60 s, a sudden

increase in filopod length is observed, ρ increases to 0.755 (Figure 5.9d). For both time ranges, filopod length correlates well with PAS values. However, the link between filopod length and PAS is yet to be determined.

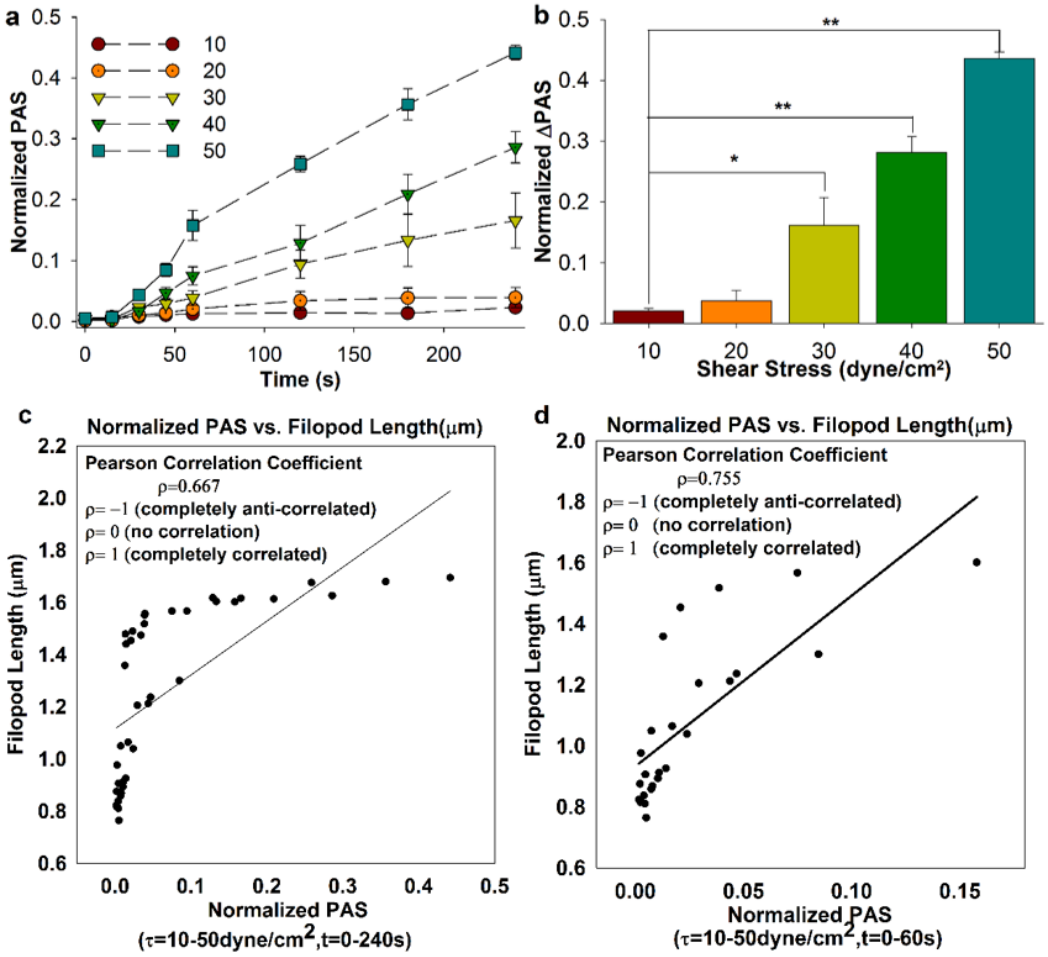

Figure 5.9: Plots of normalized PAS and Correlation between PAS and Filopodia Length. (a) Experimental observations of Normalized PAS for the various shear stress (10, 20, 30, 40 and 50 dyne cm^{-2}) and exposure time (0, 15, 30, 45, 60, 120, 180 and 240 s) combinations. (b) The difference in PAS between the 0 and 240 s samples when compared to 10 dyne cm^{-2}. Also shown is the correlation between experimental observations Filopodia length (μm) and normalized PAS for shear stress (10-50 dyne cm^{-2}) for (c) 0-240 s (ρ=0.667) and (d) 0-60 s (ρ=0.755).

Chapter 6

Conclusions and Future Work

Filopodia formation plays an important role in early stages of platelet activation [80]. Limitations in establishing a quantitative link from experimental data alone, has motivated us to design a simulation model that can represent the dynamics of filopodia formation and can be validated experimentally. However, lack of a platelet model that can be used in simulations to study the effects of shear-flow and to depict the induced dramatic platelet shape change is hindering the progress. As a first attempt, this thesis work presents a computationally feasible and deformable 3D CGMD particle-based model that helps simulate a platelet in its quiescent state and enable the dynamic filopodia formation during early stages of platelet activation.

Some significant platelet activation features were captured by this model, after overcoming many modeling and computational challenges, one of which is to maintain the integrity of the various components representing the platelet while it undergoes dramatic shape changes during the filopodia formation. By representing the intra-platelet structures with particles interacting with effective potentials, the number of degrees of freedom was reduced, allowing us to run and complete CGMD simulations on large parallelized simulation mainframes within days. By developing a comprehensive parameter system conditions, it was possible to carry out these CG simulations with considerable computational efficiency.

The model provides a compact parameter set that can be flexibly adjusted to illustrate the filopodia formation dynamics. The model's capability of characterizing diverse platelet shape changes is achieved by introducing variability in choosing one or more combinations of the 59 filament bundles used to simulate the formation of filopodia of different lengths and thicknesses. The function that maps the model parameters to observed geometric measurements in platelets was established by analyzing the numerical trends, enabling the use of formulae for simulating filopodia of varied lengths and thicknesses within the parameter space of this model. The visual realizations of the simulated filopodia formations were further compared with experimentally measured geometric features of flow-induced activated platelets. The model, along with experimental investigation, establishes a novel dynamic framework for exploring the underlying mechanism of filopodia formation and their quantitative contribution to platelet shape change. By incorporating additional key features of the molecular processes and the extra-cellular environment (blood flow, wall interaction, etc.), this model may be extended to gain a complete mechanistic description of filopodia formation and platelet shape change during activation.

The second part of this thesis investigated the platelet morphological changes in response to combined shear stress and exposure time conditions. These changes are quantified by morphometrics of the distinct features of platelets, the filopodia and central body. The growth of filopodia on platelet is described by an initial value problem based on the logistic equations that, in general, defines the growth model for any self-limiting biological systems. It is fitting to adopt such a model to express the filopodia growth on platelets that have a limited number of actin filaments.

All the parameters for the filopod length $L(\tau, t)$ were derived from conventional experiments as described in Section 5.3.1. The SEM images for the "end points" results when platelets are exposed to discrete shear stress levels (10, 20, 30, 40 and 50 dyne cm^{-2}) and exposure time points (0, 15, 30, 45, 60, 120, 180 and 240 s) were analyzed using the ImageJ software and used to determine the parameters. In addition to determining the filopodia growth model, the central body circularity was also studied. Previous works that have studied platelet shape change in response to biochemical agonists [13, 72, 137], contact with surfaces [76, 138] and fluid shear stress [73, 80, 139] have shown rounding or spreading of the central body in addition to filopodia growth. The circularity is analyzed by curve-fitting an ellipse to the boundary of the central body. The results of mean circularity and mean major axis indicate that the platelets central body maintains its circular shape under the given experimental conditions. Also, the average filopodia number is between 2-3 with 90% of filopodia number between 0-5 for platelets before and during activation caused by the given shear stress-exposure time combinations.

Several prior studies have examined platelet activation response to fluid shear stress and exposure time by measuring chemical activity modified prothrombinase activity utilized in the PAS assay [108, 133, 134, 140, 141]. The PAS assay gives a near real-time measurement of generated thrombin that does not feed back to further activate platelets. This gives the advantage of a 1:1 correlation between the agonist applied, *i.e.*, shear stress and the level of activation. The correlation between the such established response measurements given by PAS and platelet filopodia formation is studied. However, the strong correlation observed in this study does not imply a link with thrombin, as the acetylated thrombin cannot bind to the PAR receptors on the

platelets, and the commonalities between the thrombin generation pathway and triggers for platelet shape change are not yet understood.

Like with many other theoretical constructions the applicability of the filopodia growth model to reality is fairly incidental and restricted to lower shear stress levels. However, since the derived equations are in good agreement with the growth trends obtained from generally accepted experimental measurements, it seems to offer a good approximation of the actual filopodia growth on platelets by actin monomer polymerization. Future work includes using the quantitative model to advance the particle-based simulation of platelet activation, where a platelet model [142] extends filopodia in response to external shear flow conditions.

Bibliography

1. Pothapragada, S., et al., *A phenomenological particle-based platelet model for simulating filopodia formation during early activation.* International Journal for Numerical Methods in Biomedical Engineering, 2015. **31**(3): p. 1-16.

2. Pothapragada, S., et al., *A Quantitative Model for Shear Flow-Induced Platelet Morphological Changes and Corroboration with In Vitro Experiments.* Mathematical BioSciences (*Under Review, Jan 2015*).

3. Pothapragada, S. and Y. Deng. *Supercomputer simulations of platelet activation in blood plasma at multiple scales*. in *High Performance Computing & Simulation (HPCS), 2014 International Conference on*. 2014.

4. Bluestein, D., et al., *Multiscale Modeling of Flow Induced Thrombogenicity with Dissipative Particle Dynamics (Dpd) and Molecular Dynamics (Md).* Asme 2013 Conference on Frontiers in Medical Devices: Applications of Computer Modeling and Simulation, 2013. **7**(4): p. 024502.

5. Zhang, P., et al. *Multiscale Modeling of Flow Induced Thrombogenicity Using Dissipative Particle Dynamics and Coarse Grained Molecular Dynamics*. in *ASME 2013 Summer Bioengineering Conference*. 2013. American Society of Mechanical Engineers.

6. Bluestein, D., et al. *Multiscale Modeling of Flow Induced Thrombogenicity Using Dissipative Particle Dynamics and Molecular Dynamics*. in *ASME 2013 2nd Global Congress on NanoEngineering for Medicine and Biology*. 2013. American Society of Mechanical Engineers.

7. Pawlik, A.H., M. Milosavljevic, and V. Bromm, *The First Galaxies: Assembly under Radiative Feedback from the First Stars.* Astrophysical Journal, 2013. **767**(1).

8. Dill, K.A. and J.L. MacCallum, *The protein-folding problem, 50 years on.* Science, 2012. **338**(6110): p. 1042-1046.

9. Garber, L., *IBM Sequoia Is World's Fastest Supercomputer.* Computer, 2012. **45**(8): p. 21-21.

10. Johnsen, P., et al., *Petascale WRF Simulation of Hurricane Sandy Deployment of NCSA's Cray XE6 Blue Waters.* 2013 International Conference for High Performance Computing, Networking, Storage and Analysis (Sc), 2013.

11. Helias, M., et al., *Supercomputers ready for use as discovery machines for neuroscience.* Frontiers in neuroinformatics, 2012. **6**.

12. Kumar, P. and M. Clark, *From Haematological Disease.* Clinical Medicine, 2005: p. 353-414.

13. Hartwig, J.H., *The platelet: Form and function.* Seminars in Hematology, 2006. **43**(1): p. S94-S100.

14. White, J.G., *Platelet Structure.* Platelets, 2nd Edition, 2007. **2**: p. 45-73.

15. Hartwig, J.H. and M. Desisto, *The Cytoskeleton of the Resting Human Blood-Platelet - Structure of the Membrane Skeleton and Its Attachment to Actin-Filaments.* Journal of Cell Biology, 1991. **112**(3): p. 407-425.

16. Hartwig, J.H., *Mechanisms of Actin Rearrangements Mediating Platelet Activation.* Journal of Cell Biology, 1992. **118**(6): p. 1421-1442.

17. McKenzie, S.B., *Clinical laboratory hematology*. Vol. 1. 2004: Prentice Hall.

18. Reichert, W.M., *Indwelling neural implants: strategies for contending with the in vivo environment*. 2007: CRC Press.

19. Caro, C., T. Pedley, and R. Schroter, *Seed WA The Mechanics of the Circulation*. 1978, Oxford: Oxford University Press.

20. Lowe, G.D., *Virchow's triad revisited: abnormal flow.* Pathophysiology of haemostasis and thrombosis, 2003. **33**(5-6): p. 455-457.

21. Bluestein, D., K.B. Chandran, and K.B. Manning, *Towards Non-thrombogenic Performance of Blood Recirculating Devices.* Annals of Biomedical Engineering, 2010. **38**(3): p. 1236-1256.

22. Christiansen, S., A. Klocke, and R. Autschbach, *Past, Present, and Future of Long-Term Mechanical Cardiac Support in Adults.* Journal of Cardiac Surgery, 2008. **23**(6): p. 664-676.

23. AlMomani, T.D.J., *Micro-scale dynamic simulation of erythrocyte-platelet interaction*. 2007: THE UNIVERSITY OF IOWA.

24. Wootton, D.M. and D.N. Ku, *Fluid mechanics of vascular systems, diseases, and thrombosis.* Annual Review of Biomedical Engineering, 1999. **1**: p. 299-329.

25. Clemetson, K.J. and J.M. Clemetson, *Chapter 6 - Platelet receptors*, in *Platelets (Second Edition)*, A.D. Michelson, Editor. 2007, Academic Press: Burlington. p. 117-143.

26. Hellums, J.D., et al., *Studies on the Mechanisms of Shear-Induced Platelet Activation*, in *Cerebral Ischemia and Hemorheology*, A. Hartmann and W. Kuschinsky, Editors. 1987, Springer Berlin Heidelberg. p. 80-89.

27. Hellums, J.D., *1993 Whitaker Lecture - Biorheology in Thrombosis Research.* Annals of Biomedical Engineering, 1994. **22**(5): p. 445-455.

28. Yoganathan, A.P., K.B. Chandran, and F. Sotiropoulos, *Flow in prosthetic heart valves: State-of-the-art and future directions.* Annals of Biomedical Engineering, 2005. **33**(12): p. 1689-1694.

29. Miller, T.F. and D.C. Clary, *Quantum free energies of the conformers of glycine on an ab initio potential energy surface.* Physical Chemistry Chemical Physics, 2004. **6**(10): p. 2563-2571.

30. Jensen, F., *Introduction to computational chemistry*. 2013: John Wiley & Sons.

31. Schlick, T., *Molecular Modeling and Simulation: An Interdisciplinary Guide: An Interdisciplinary Guide*. Vol. 21. 2010: Springer Science & Business Media.

32. Tieleman, D.P., *Computer simulations of transport through membranes: Passive diffusion, pores, channels and transporters.* Clinical and Experimental Pharmacology and Physiology, 2006. **33**(10): p. 893-903.

33. Voth, G.A., *Coarse-graining of condensed phase and biomolecular systems*. 2008: CRC press.

34. Soper, A.K., *Empirical potential Monte Carlo simulation of fluid structure.* Chemical Physics, 1996. **202**(2-3): p. 295-306.

35. Noid, W.G., et al., *The multiscale coarse-graining method. I. A rigorous bridge between atomistic and coarse-grained models.* Journal of Chemical Physics, 2008. **128**(24): p. 244114.

36. Izvekov, S., et al., *Effective force fields for condensed phase systems from ab initio molecular dynamics simulation: A new method for force-matching.* Journal of Chemical Physics, 2004. **120**(23): p. 10896-10913.

37. Cooke, I.R., K. Kremer, and M. Deserno, *Tunable generic model for fluid bilayer membranes.* Phys Rev E Stat Nonlin Soft Matter Phys, 2005. **72**(1 Pt 1): p. 011506.

38. Miyazawa, S. and R.L. Jernigan, *Residue-residue potentials with a favorable contact pair term and an unfavorable high packing density term, for simulation and threading.* Journal of Molecular Biology, 1996. **256**(3): p. 623-644.

39. Marrink, S.J., et al., *The MARTINI force field: Coarse grained model for biomolecular simulations.* Journal of Physical Chemistry B, 2007. **111**(27): p. 7812-7824.

40. Ripoll, M., M.H. Ernst, and P. Espanol, *Large scale and mesoscopic hydrodynamics for dissipative particle dynamics.* Journal of Chemical Physics, 2001. **115**(15): p. 7271-7284.

41. Espanol, P. and M. Revenga, *Smoothed dissipative particle dynamics.* Physical Review E, 2003. **67**(2): p. 026705.

42. Berendsen, H.J., *Simulating the physical world: hierarchical modeling from quantum mechanics to fluid dynamics*. 2007: Cambridge University Press.

43. Hess, B., et al., *GROMACS 4: Algorithms for highly efficient, load-balanced, and scalable molecular simulation.* Journal of Chemical Theory and Computation, 2008. **4**(3): p. 435-447.

44. Seiler, M.C. and F.A. Seiler, *Numerical recipes in C: the art of scientific computing.* Risk Analysis, 1989. **9**(3): p. 415-416.

45. Phillips, J.C., et al., *Scalable molecular dynamics with NAMD.* Journal of Computational Chemistry, 2005. **26**(16): p. 1781-1802.

46. Kumar, S., et al., *Scalable molecular dynamics with NAMD on the IBM Blue Gene/L system.* Ibm Journal of Research and Development, 2008. **52**(1-2): p. 177-188.

47. Plimpton, S., *Fast Parallel Algorithms for Short-Range Molecular-Dynamics.* Journal of Computational Physics, 1995. **117**(1): p. 1-19.

48. Humphrey, W., A. Dalke, and K. Schulten, *VMD: Visual molecular dynamics.* Journal of Molecular Graphics & Modelling, 1996. **14**(1): p. 33-38.

49. Burks, A.W., H.H. Goldstine, and J. von Neumann, *Preliminary Discussion of the Logical Design of an Electronic Computing Instrument.* The Institute for Advanced Study, 1946.

50. Fermi, E., N. Metropolis, and E.F. Alei, *Phase Shift Analysis of the Scattering of Negative Pions by Hydrogen.* Physical Review, 1954. **95**(6): p. 1581-1585.

51. Gamow, G., *Possible Relation between Deoxyribonucleic Acid and Protein Structures.* Nature, 1954. **173**(4398): p. 318-318.

52. Metropolis, N., et al., *Equation of State Calculations by Fast Computing Machines.* Journal of Chemical Physics, 1953. **21**(6): p. 1087-1092.

53. Metropolis, N. and S. Ulam, *The Monte Carlo Method.* Journal of the American Statistical Association, 1949. **44**(247): p. 335-341.

54. Alder, B.J. and T. Wainwright, *Molecular Dynamics by electronic computers.* Proceedings of the International Symposium on Transport Processes in Statistical Mechanics, Brussels,1956, Interscience Publishers, Inc., New York, August 27–31,1958: p. 97-131.

55. Rahman, A., *Correlations in Motion of Atoms in Liquid Argon.* Physical Review a-General Physics, 1964. **136**(2A): p. A405-&.

56. Ritchie, D.M., B.W. Kernighan, and M.E. Lesk, *The C programming language*. 1975: Bell Laboratories.

57. Top500., *Top 500 Supercomputer Site. Available from: http://www.top500.org*.

58. Dongarra, J.J., P. Luszczek, and A. Petitet, *The LINPACK benchmark: past, present and future.* Concurrency and Computation-Practice & Experience, 2003. **15**(9): p. 803-820.

59. Fogelson, A.L., *A Mathematical-Model and Numerical-Method for Studying Platelet-Adhesion and Aggregation during Blood-Clotting.* Journal of Computational Physics, 1984. **56**(1): p. 111-134.

60. Wang, N.T. and A.L. Fogelson, *Computational methods for continuum models of platelet aggregation.* Journal of Computational Physics, 1999. **151**(2): p. 649-675.

61. Kamada, H., et al., *A three-dimensional particle simulation of the formation and collapse of a primary thrombus.* International Journal for Numerical Methods in Biomedical Engineering, 2010. **26**(3-4): p. 488-500.

62. Huang, P.Y. and J.D. Hellums, *Aggregation and Disaggregation Kinetics of Human Blood-Platelets .1. Development and Validation of a Population Balance Method.* Biophysical Journal, 1993. **65**(1): p. 334-343.

63. Tandon, P. and S.L. Diamond, *Hydrodynamic effects and receptor interactions of platelets and their aggregates in linear shear flow.* Biophysical Journal, 1997. **73**(5): p. 2819-2835.

64. Maul, C., et al., *Sedimentation of Hexagonal Flakes in a Half-Space - Numerical Predictions and Experiments in Stokes-Flow.* Journal of Imaging Science and Technology, 1994. **38**(3): p. 241-248.

65. Mody, N.A., et al., *Mechanics of transient platelet adhesion to von Willebrand factor under flow*. Biophysical Journal, 2005. **88**(2): p. 1432-1443.

66. Crowl, L.M. and A.L. Fogelson, *Computational model of whole blood exhibiting lateral platelet motion induced by red blood cells.* International Journal for Numerical Methods in Biomedical Engineering, 2010. **26**(3-4): p. 471-487.

67. Pozrikidis, C., *Flipping of an adherent blood platelet over a substrate.* Journal of Fluid Mechanics, 2006. **568**: p. 161-172.

68. Mody, N.A. and M.R. King, *Platelet adhesive dynamics. Part I: Characterization of platelet hydrodynamic collisions and wall effects.* Biophysical Journal, 2008. **95**(5): p. 2539-2555.

69. Wang, W.W., N.A. Mody, and M.R. King, *Multiscale model of platelet translocation and collision.* Journal of Computational Physics, 2013. **244**: p. 223-235.

70. Sweet, C.R., et al., *Modelling platelet-blood flow interaction using the subcellular element Langevin method*. Journal of Royal Society Interface, 2011. **8**(65): p. 1760-71.

71. Frojmovic, M., K. Longmire, and T.G.M. Vandeven, *Long-Range Interactions in Mammalian Platelet-Aggregation .2. The Role of Platelet Pseudopod Number and Length.* Biophysical Journal, 1990. **58**(2): p. 309-318.

72. Hensler, M.E., et al., *Platelet Morphological-Changes and Fibrinogen Receptor Localization - Initial Responses in Adp-Activated Human Platelets.* American Journal of Pathology, 1992. **141**(3): p. 707-719.

73. Kuwahara, M., et al., *Platelet shape changes and adhesion under high shear flow.* Arteriosclerosis Thrombosis and Vascular Biology, 2002. **22**(2): p. 329-334.

74. Lee, D., et al., *Differential Dynamics of Platelet Contact and Spreading.* Biophysical Journal, 2012. **102**(3): p. 472-482.

75. Posch, S., et al., *Activation induced morphological changes and integrin alpha IIb beta 3 activity of living platelets.* Methods, 2013. **60**(2): p. 179-185.

76. Kraus, M.J., E.F. Strasser, and R. Eckstein, *A New Method for Measuring the Dynamic Shape Change of Platelets.* Transfusion Medicine and Hemotherapy, 2010. **37**(5): p. 306-310.

77. Dror, R.O., et al., *Biomolecular Simulation: A Computational Microscope for Molecular Biology.* Annual Review of Biophysics, Vol 41, 2012. **41**: p. 429-452.

78. Riniker, S., J.R. Allison, and W.F. van Gunsteren, *On developing coarse-grained models for biomolecular simulation: a review.* Physical Chemistry Chemical Physics, 2012. **14**(36): p. 12423-12430.

79. Yamaoka, H., et al., *Multiscale modeling and mechanics of filamentous actin cytoskeleton.* Biomechanics and Modeling in Mechanobiology, 2012. **11**(3-4): p. 291-302.

80. Ajzenberg, N., et al., *Platelet shape change and subsequent glycoprotein redistribution in human stenosed arteries.* Platelets, 2005. **16**(1): p. 13-8.

81. Ujihara, Y., et al., *Proposed Spring Network Cell Model Based on a Minimum Energy Concept.* Annals of Biomedical Engineering, 2010. **38**(4): p. 1530-1538.

82. Dzwinel, W., K. Boryczko, and D.A. Yuen, *A discrete-particle model of blood dynamics in capillary vessels.* Journal of Colloid and Interface Science, 2003. **258**(1): p. 163-173.

83. Fedosov, D.A., B. Caswell, and G.E. Karniadakis, *A Multiscale Red Blood Cell Model with Accurate Mechanics, Rheology, and Dynamics.* Biophysical Journal, 2010. **98**(10): p. 2215-2225.

84. Noguchi, H. and G. Gompper, *Shape transitions of fluid vesicles and red blood cells in capillary flows.* Proceedings of the National Academy of Sciences of the United States of America, 2005. **102**(40): p. 14159-14164.

85. Pivkin, I.V. and G.E. Karniadakis, *Accurate coarse-grained modeling of red blood cells.* Physical Review Letters, 2008. **101**(11): p. 118105.

86. Discher, D.E., D.H. Boal, and S.K. Boey, *Simulations of the erythrocyte cytoskeleton at large deformation. II. Micropipette aspiration.* Biophysical Journal, 1998. **75**(3): p. 1584-1597.

87. Persson, P.O. and G. Strang, *A simple mesh generator in MATLAB.* Siam Review, 2004. **46**(2): p. 329-345.

88. Mogilner, A. and B. Rubinstein, *The physics of filopodial protrusion.* Biophysical Journal, 2005. **89**(2): p. 782-795.

89. Schirenbeck, A., et al., *The bundling activity of vasodilator-stimulated phosphoprotein is required for filopodium formation.* Proceedings of the National Academy of Sciences of the United States of America, 2006. **103**(20): p. 7694-7699.

90. Lan, Y.H. and G.A. Papoian, *The stochastic dynamics of filopodial growth.* Biophysical Journal, 2008. **94**(10): p. 3839-3852.

91. Zhuravlev, P.I. and G.A. Papoian, *Molecular noise of capping protein binding induces macroscopic instability in filopodial dynamics.* Proceedings of the National Academy of Sciences of the United States of America, 2009. **106**(28): p. 11570-11575.

92. Kim, T., W. Hwang, and R.D. Kamm, *Computational Analysis of a Cross-linked Actin-like Network.* Experimental Mechanics, 2009. **49**(1): p. 91-104.

93. Gardel, M.L., et al., *Elastic behavior of cross-linked and bundled actin networks.* Science, 2004. **304**(5675): p. 1301-5.

94. Takatsuki, H., E. Bengtsson, and A. Mansson, *Persistence length of fascin-cross-linked actin filament bundles in solution and the in vitro motility assay.* Biochimica Et Biophysica Acta-General Subjects, 2014. **1840**(6): p. 1933-1942.

95. Claessens, M.M., et al., *Actin-binding proteins sensitively mediate F-actin bundle stiffness.* Nat Mater, 2006. **5**(9): p. 748-53.

96. Hosseini, S.M. and J.J. Feng, *A particle-based model for the transport of erythrocytes in capillaries.* Chemical Engineering Science, 2009. **64**(22): p. 4488-4497.

97. Allen, M.P. and D.J. Tildesley, *Computer simulation of liquids*. 1989: Clarendon Press. 385.

98. Kojima, H., A. Ishijima, and T. Yanagida, *Direct Measurement of Stiffness of Single Actin-Filaments with and without Tropomyosin by in-Vitro Nanomanipulation.* Proceedings of the National Academy of Sciences of the United States of America, 1994. **91**(26): p. 12962-12966.

99. Higuchi, H., T. Yanagida, and Y.E. Goldman, *Compliance of Thin-Filaments in Skinned Fibers of Rabbit Skeletal-Muscle.* Biophysical Journal, 1995. **69**(3): p. 1000-1010.

100. Bertaud, J., Z. Qin, and M.J. Buehler, *Intermediate filament-deficient cells are mechanically softer at large deformation: a multi-scale simulation study.* Acta Biomater, 2010. **6**(7): p. 2457-66.

101. Nikunen, P., M. Karttunen, and I. Vattulainen, *How would you integrate the equations of motion in dissipative particle dynamics simulations?* Computer Physics Communications, 2003. **153**(3): p. 407-423.

102. Ciesla, M., J. Pawlowicz, and L. Longa, *Molecular dynamics simulation of the lennard-jones polymers in a good solvent.* Acta Physica Polonica B, 2007. **38**(5): p. 1727-1736.

103. Schmidt, R.R., J.G.H. Cifre, and J.G. de la Torre, *Comparison of Brownian dynamics algorithms with hydrodynamic interaction.* Journal of Chemical Physics, 2011. **135**(8): p. 084116.

104. Haga, J.H., et al., *Quantification of the passive mechanical properties of the resting platelet.* Annals of biomedical engineering, 1998. **26**(2): p. 268-77.

105. Bolin, R.B., et al., *Buoyant Density of Platelets Stored at Room-Temperature as Platelet Concentrates.* Journal of Laboratory and Clinical Medicine, 1981. **98**(3): p. 342-351.

106. Plimpton, S., A. Thompson, and P. Crozier. *LAMMPS Molecular Dynamics Simulator*. 2012; Available from: http://lammps.sandia.gov.

107. Jesty, J. and D. Bluestein, *Acetylated prothrombin as a substrate in the measurement of the procoagulant activity of platelets: elimination of the feedback activation of platelets by thrombin.* Analytical Biochemistry, 1999. **272**(1): p. 64-70.

108. Schulz-Heik, K., et al., *The extent of platelet activation under shear depends on platelet count: Differential expression of anionic phospholipid and factor Va.* Pathophysiology of Haemostasis and Thrombosis, 2005. **34**(6): p. 255-262.

109. Sheriff, J., et al., *High-Shear Stress Sensitizes Platelets to Subsequent Low-Shear Conditions.* Annals of biomedical engineering, 2010. **38**(4): p. 1442-1450.

110. Go, A.S., et al., *Heart Disease and Stroke Statistics-2014 Update A Report From the American Heart Association.* Circulation, 2014. **129**(3): p. E28-E292.

111. Lazar, R.M., et al., *Neurological events during long-term mechanical circulatory support for heart failure - The Randomized Evaluation of Mechanical Assistance for the Treatment of Congestive Heart Failure (REMATCH) experience.* Circulation, 2004. **109**(20): p. 2423-2427.

112. Yoganathan, A.P., et al., *Fluid dynamic studies for the year 2000.* Journal of Heart Valve Disease, 1998. **7**(2): p. 130-139.

113. Healy, T.M., et al., *An automated method for analysis and visualization of laser Doppler velocimetry data.* Annals of Biomedical Engineering, 1997. **25**(2): p. 335-343.

114. Ramstack, J.M., L. Zuckerman, and L.F. Mockros, *Shear-induced activation of platelets.* J Biomech, 1979. **12**(2): p. 113-25.

115. Sutera, S.P. and M.H. Mehrjardi, *Deformation and fragmentation of human red blood cells in turbulent shear flow*. Biophys J, 1975. **15**(1): p. 1-10.

116. Bluestein, D., *Towards optimization of the thrombogenic potential of blood recirculating cardiovascular devices using modeling approaches.* Expert Rev Med Devices, 2006. **3**(3): p. 267-70.

117. Bluestein, D., K.B. Chandran, and K.B. Manning, *Towards non-thrombogenic performance of blood recirculating devices.* Ann Biomed Eng, 2010. **38**(3): p. 1236-56.

118. Blackshear, P.L., Jr., F.D. Dorman, and J.H. Steinbach, *Some Mechanical Effects That Influence Hemolysis.* Trans Am Soc Artif Intern Organs, 1965. **11**: p. 112-7.

119. Wurzinger, L.J., et al., *Platelet and Coagulation Parameters Following Millisecond Exposure to Laminar Shear-Stress.* Thrombosis and Haemostasis, 1985. **54**(2): p. 381-386.

120. Kroll, M.H., et al., *Platelets and shear stress.* Blood, 1996. **88**(5): p. 1525-41.

121. Boreda, R., R. Fatemi, and S. Rittgers, *Potential for platelet stimulation in critically stenosed carotid and coronary arteries.* J Vasc Invest, 1995. **1**(1): p. 26-37.

122. Giersiepen, M., et al., *Estimation of shear stress-related blood damage in heart valve prostheses--in vitro comparison of 25 aortic valves.* Int J Artif Organs, 1990. **13**(5): p. 300-6.

123. Wu, J.S., et al., *Numerical Investigation of the Effects of Channel Geometry on Platelet Activation and Blood Damage.* Annals of Biomedical Engineering, 2011. **39**(2): p. 897-910.

124. Bluestein, D., et al., *Fluid mechanics of arterial stenosis: Relationship to the development of mural thrombus.* Annals of Biomedical Engineering, 1997. **25**(2): p. 344-356.

125. Dumont, K., et al., *Comparison of the hemodynamic and thrombogenic performance of two bileaflet mechanical heart valves using a CFD/FSI model.* Journal of Biomechanical Engineering-Transactions of the Asme, 2007. **129**(4): p. 558-565.

126. Tambasco, M. and D.A. Steinman, *Path-dependent hemodynamics of the stenosed carotid bifurcation.* Annals of Biomedical Engineering, 2003. **31**(9): p. 1054-1065.

127. Bluestein, D., et al., *Flow-induced platelet activation in mechanical heart valves.* Journal of Heart Valve Disease, 2004. **13**(3): p. 501-508.

128. Mejillano, M.R., et al., *Lamellipodial versus filopodial mode of the actin nanomachinery: Pivotal role of the filament barbed end.* Cell, 2004. **118**(3): p. 363-373.

129. Hartwig, J.H., et al., *The elegant platelet: Signals controlling actin assembly.* Thrombosis and Haemostasis, 1999. **82**(2): p. 392-398.

130. Verhulst, P.-F., *Recherches mathématiques sur la loi d'accroissement de la population.* Nouveaux mémoires de l'académie royale des sciences et belles-lettres de Bruxelles, 1845. **18**: p. 14-54.

131. Hey, A.J., S. Tansley, and K.M. Tolle, *The fourth paradigm: data-intensive scientific discovery.* 2009.

132. Yin, W., et al., *Flow-induced platelet activation in bileaflet and monoleaflet mechanical heart valves.* Annals of Biomedical Engineering, 2004. **32**(8): p. 1058-1066.

133. Jesty, J., et al., *Platelet activation in a circulating flow loop: combined effects of shear stress and exposure time.* Platelets, 2003. **14**(3): p. 143-9.

134. Sheriff, J., et al., *High-Shear Stress Sensitizes Platelets to Subsequent Low-Shear Conditions.* Ann. Biomed. Eng., 2010. **38**(4): p. 1442-1450.

135. Xenos, M., et al., *Device Thrombogenicity Emulator (DTE) - Design optimization methodology for cardiovascular devices: A study in two bileaflet MHV designs.* Journal of Biomechanics, 2010. **43**(12): p. 2400-2409.

136. Schneider, C.A., W.S. Rasband, and K.W. Eliceiri, *NIH Image to ImageJ: 25 years of image analysis.* Nature Methods, 2012. **9**(7): p. 671-675.

137. Kraus, M.-J., H. Neeb, and E.F. Strasser, *Fractal and Euclidean descriptors of platelet shape.* Platelets, 2013. **25**(0): p. 1-11.

138. Ikeda, M., et al., *Simultaneous digital imaging analysis of cytosolic calcium and morphological change in platelets activated by surface contact (vol 61, pg 292, 1996).* Journal of Cellular Biochemistry, 1996. **62**(1): p. U3-U4.

139. Maxwell, M.J., et al., *Shear induces a unique series of morphological changes in translocating platelets - Effects of morphology on translocation dynamics.* Arteriosclerosis Thrombosis and Vascular Biology, 2006. **26**(3): p. 663-669.

140. Yin, W., S.K. Shanmugavelayudam, and D.A. Rubenstein, *The effect of physiologically relevant dynamic shear stress on platelet and endothelial cell activation.* Thrombosis Research, 2011. **127**(3): p. 235-241.

141. Sheriff, J., et al., *Evaluation of Shear-Induced Platelet Activation Models Under Constant and Dynamic Shear Stress Loading Conditions Relevant to Devices.* Annals of Biomedical Engineering, 2013. **41**(6): p. 1279-1296.

142. Pothapragada, S., et al., *A phenomenological particle-based platelet model for simulating filopodia formation during early activation.* International Journal for Numerical Methods in Biomedical Engineering, 2014, (*To Appear*). p. n/a-n/a.